Title
Synthesis and characterization of magnetically-switchable cobalt-containing nanoparticles

Author
Gill-Ljunghammer, Sasha Lenore

Publication Date
2022

Peer reviewed|Thesis/dissertation

UNIVERSITY OF CALIFORNIA

Los Angeles

Synthesis and Characterization of Magnetically-Switchable Cobalt-Containing Nanoparticles

A thesis submitted in partial satisfaction

of the requirements for the degree Master of Science

in Chemistry

by

Sasha Lenore Gill-Ljunghammer

2022

ABSTRACT OF THE THESIS

Synthesis and Characterization

of Magnetically-Switchable

Cobalt-Containing Nanoparticles

by

Sasha Lenore Gill-Ljunghammer

Master of Science in Chemistry

University of California, Los Angeles, 2022

Professor Sarah H. Tolbert, Chair

As electronic devices become more integrated in everyday life, there is an increasing necessity for miniaturization with exceptional efficiency. The use of tunable magnetic materials for information storage and transfer can meet this demand with many significant advantages over current technologies. The implementation of this science is contingent on optimizing the voltage control of magnetism (VCM), which has additional applications in healthcare and sensing. This work seeks to improve VCM in multiferroic composites and magnetoioics. In chapter 3 of this thesis, we report a straightforward and scalable synthesis of superparamagnetic cobalt ferrite nanoparticles that allows for precise size selection. The particles produced via this route also have remarkable size and shape uniformity, making them ideal for use in a strain-mediated multiferroic composite. In chapter 4 we advance fundamental understanding toward achieving unprecedented magnetic control in

nanostructured Sm-Co magnets via electrochemical hydrogen charging. The structural and magnetic properties of $SmCo_5$ and Sm_2Co_{17}, as well as the kinetics and thermodynamics involved in their hydrogenation, are documented for future work. Oxidation in air and in electrolyte is identified as a key challenge.

The thesis of Sasha Lenore Gill-Ljunghammer is approved.

Chong Liu

Gregory P Carman

Sarah H. Tolbert, Committee Chair

University of California, Los Angeles

2022

TABLE OF CONTENTS

TABLE OF FIGURES

ACKNOWLEDGEMENTS

This work could not have been possible without the overwhelming support I have received throughout my academic career.

First and foremost, I would like to thank my research advisor, Sarah Tolbert, for taking a chance on me and giving me every opportunity to excel.

Thank you to my graduate student mentors Jeffery Kurish, Shreya Patel and Ryan Dodson for always fostering my curiosity.

I am incredibly grateful for the funding and professional development that I have received from the Beckman Scholars Program. The same goes for the Translational Applications of Nanoscale Multiferroic Systems Undergraduate Research Program.

Much of the work presented in chapter three was completed in collaboration with Jeffrey Kurish, Katherine Estoque, and Shreya Patel.

The incredibly insightful XPS data presented in chapter 4 was collected by Casey Cornwell, who has always been an exceptionally helpful lab mate.

Finally, I acknowledge the American Chemical Society for allowing me to publish work from *J. Am. Chem. Soc.* **2019**, *141*, 7037-7045 and *Chem. Rev.* **2021** DOI: 10.1021/acs.chemrev.1c00860 as well as Springer Nature for reprint rights for work in *Nature*. **2001**, *414*, 353-358 and *J. Mater. Sci.* **1985**, *20*, 817-820.

Chapter 1: Voltage control of magnetism

1.1 An internet of things

The last few decades have seen a technological explosion in devices capable of information storage and transfer. These are the smartphones, laptops, and sensors that have come to permeate every aspect of our daily lives and take up key roles in our industries and infrastructures. The increasing connectivity of these devices has scaled exponentially with the data processing power required to support their connections, to form what is known as the internet of things (IoT).[1] This incorporation of computing systems into the physical world in the IoT, along with artificial intelligence (AI) and machine learning (ML), is leading the charge in demanding ever faster and more efficient information processors.

1.2 The end of Moore's law

Efforts to improve computational speed and efficiency have been led by miniaturization. For roughly 40 years, this was mainly achieved by shrinking metal-oxide-semiconductor field-effect transistors (MOSFETs). These devices have famously followed a trend known as Moore's Law, which predicted a 50% decrease in transistor sizes approximately every two years. Recently, however, technological advancement via MOSFET miniaturization has begun to stagnate as we are confronted with the end of Moore's Law.

The inevitable breakdown of Moore's Law is due to several factors. The first being that transistors are arriving at their smallest physical limit before quantum effects begin wreaking havoc.[2] Transistors operate by controlling a current flow across small gates, which are only ~10 atoms wide in today's smallest MOSFETs. At these nanometer scales, quantum tunneling may cause data corruption. Furthermore, increasing the number of transistors on a chip also increases the amount of heat the chip produces, which is not only an energy drain, but is also harmful to the surrounding computer hardware.[3]

Although some argue that Moore's Law has not reached its end, the gross energy consumption required by MOSFETs in an increasingly digitalized age cannot go unaddressed regardless. If we continue primarily using MOSFETs for logic operations through the expansion of the IoT, AI, and ML; it is predicted that the power consumed by microelectronics will go from 5% of the world's total power consumption, to 20% of our total power consumption by 2030.[4] This has left scientists to search for creative adaptations or alternatives to the common MOSFET– many believe that the solution may lie in a different property of electrons - spin.

1.3 The birth of magnetic memory storage

Rather than operating on the translational movement of electrons to store memory, magnetic memory storage relies on the manipulation of an electron spin magnetic moment. The moments could be controlled by applying an external magnetic field, but this is incredibly energy costly. Instead, most early research into magnetic memory storage explored current-controlled magnetism. While this was more practical than the control via an external electric field, losses due to Joule heating brought up efficiency challenges. Finally, focus shifted toward to voltage control of magnetism (VCM). The remainder of this chapter will give a brief overview of the most common methods to achieving VCM.

1.4 VCM methods

1.4.1 Single-phase magnetoelectric materials and multiferroics

The magnetoelectric (ME) effect refers to the coupling of magnetic and electronic behavior. Materials that produce a magnetic moment as a result of an externally applied electric field or produce an electronic moment as a result of an externally applied magnetic field are said to be magnetoelectric. One of the first ME materials discovered was single-phase Cr_2O_3, an antiferromagnet.[5,6]

While this exciting discovery sparked intense research efforts into MEs, the magnitude of the induced magnetization or polarization was far below what would be required in practical application. This weak response in Cr_2O_3 is because there are very few ferromagnetically coupled spins in antiferromagnets, and these are what cause the ME response.[7] For this reason, research efforts sought to discover ferromagnetic materials that exhibited the ME effect. These materials, known as magnetoelectric multiferroics (ME MFs), are both ferroelectric and ferromagnetic.

Since this push, many single-phase ME MFs have been uncovered. These most notably include yttrium iron garnet (YIG) and $TbPO_4$.[8,9] Although ME MFs show more dramatic responses to applied magnetic and electric fields than non-ferromagnetic MEs, the polarization and magnetizations were still too small to be useful. Furthermore, due to the unlikely physics of ferroelectricity and ferromagnetism coinciding (ferroelectricity mostly occurs in materials with empty *d* orbitals while ferromagnetism requires unpaired *d* electrons), ME MFs are scarce and often require cryogenic temperatures to maintain their ordering.[10] As a result, scientists were left to develop more creative materials to actualize the voltage-control of magnetism in devices. This gave way to one of the most widely explored avenues of VCM – multiferroic composites.

1.4.2 Strain-mediated VCM in multiferroic composites

Rather than relying on one material with both intrinsic ferroelectricity and ferromagnetism, strain-mediated multiferroic composites connect a ferroelectric material with a ferromagnetic material through their elastic interaction. The ferroelectric material in question must be a piezoelectric, meaning that it distorts upon being polarized or it becomes polarized when a strain is applied to it. Simultaneously, the ferromagnet must experience magnetic changes due to strain - a property known as magnetostriction. This can be used in the fabrication of voltage-controlled magnetic devices on the working principle that an applied bias will induce a deformation of the piezoelectric, which in turn strains the coupled ferromagnet, resulting in a change in magnetization.

The development of strain-mediated multiferroic composites led to a new boom in magnetoelectric materials research. These highly tunable devices are capable of room temperature magnetic changes five orders of magnitude greater than single-phase MEs.[10] Many applications now actively employ this technology in data storage, attenuators, and filters.

1.4.3 Charge carrier doping

Devices that allow for VCM via charge carrier doping are made up of a polarizable liquid or solid that is sandwiched between two electrodes – one magnetic and the other not necessarily so. The application of a bias across this sandwich results in the polarization of the central material. This polarization in turn attracts the accumulation of electrons or holes in the magnetic working electrode at the gating interface. These changes in electronic structure also impact the electrode's magnetism. This relationship was first explored in semiconductor materials like (In,Mn)As, which were capable of transitioning from a ferromagnetic to paramagnetic state.[11] However, the use of semiconductors in real-world VCM devices is impractical since their ferromagnetism is only stable below ~100 K.[10]

Unlike semiconductors, metals have very high Curie temperatures, making them attractive candidates for further developments in charge doping VCM. Impressive changes in anisotropy have been observed in devices using ultrathin films of iron and cobalt but progress with charge carrier doping of metals has stagnated due to the high electric field screening of metals preventing charge accumulation beyond a few atomic layers.[12]

1.4.4 Magnetoionics

The next development in VCM technology operates on a similar principle as batteries. By harnessing ionic intercalation, magnetoionics are capable of manipulating magnetism in the bulk. This can be achieved with liquid electrolytes through which ions, such as Li^{+}or O^{2-}, intercalate and deintercalated into magnetic crystal lattices where they cause changes in electronic and magnetic ordering.[10] It is also possible for magnetoionics to operate on ionic mobility through solid-state, as is seen in

Co/GdO_x heterostructures.[13] Regardless of whether the magnetoionic device is all-solid-state or a liquid/solid composite, the ability to access and influence such large volumes of magnetic material has brought about unprecedented magnetic changes.

Still, some concerns have arisen about reversibility in magnetoionics due to the possibility of intercalation-induced electrode degradation.[14] The attractive stability of metals also remains just out of reach of magnetoionics because electric field screening limits the penetration of charged ions to any considerable depth.

While the scope of VCM research is broader than what has been briefly encapsulated here, this chapter has served to argue the necessity of VCM, and to provide a picture of its main approaches and their limitations. In this thesis, we make contributions to two areas within this field - namely, strain-mediated multiferroics and a more recent magnetoionic-like avenue.

1.5 References

(1) Ramesh, R.; Martin, L.W. *Riv. Nuovo Cim.* **2021**, *44*, 251–289.

(2) Theis, T. N.; Wong, S. P. *Comput. Sci. Eng.* **2017**, *19*, 41-50.

(3) Waldrop, M. M. *Nature News* **2016**, *530.7589*, 144.

(4) Adapted from, gadgets and gigawatts, policies for energy efficient electronics, *International Energy Agency* **2009**

(5) Astrov, D. N. *Sov. Phys.-JETP* **1961**, *13*, 729.

(6) Folen V. J.; Rado, G. T. E. W. Stalder, *Phys. Rev. Lett.* **1961**, *6*, 607.

(7) Rado, G. T.; Folen V. J. *Phys. Rev. Lett.* **1961**, *7*, 310.

(8) Krichevtsov, B. B.; Pavlov, V. V.; Pisarev, R. V. *JETP Lett.* **1989**, *49*, 535.

(9) Rado, G. T.; Ferrari, J. M.; Maisch, W. G. *Phys. Rev. B* **1984** *29*, 4041.

(10) Molinari, A.; Hahn, H.; Kruk, R. *Adv. Mater.* **2019**, *31*, 1880662.

(11) Ohno, H.; Chiba, D.; Matsukura, F.; Omiya, T.; Abe, E.; Dietl,T.; Ohno, Y.; Ohtani, K. *Nature* **2000**, *408*, 944.

(12) Maruyama, T.; Shiota,Y.; Nozaki, T.; Ohta, K.; Toda, N.; Mizuguchi, N.; Tulapurkar, A.; Shinjo, T.; Shiraishi, M.; Mizukami, S.; Ando, Y.; Suzuki, Y. *Nat. Nanotechnol.* **2009**, *4*, 158.

(13) Bauer, U.; Yao, L.; Tan, A. J.; Agrawal, P.; Emori, S.; Tuller, H. L.; van Dijken, S.; Beach, G. S. D. *Nat. Mater.* **2015**, *14*, 174.

(14) Zhang, Q. *et al. Nano Lett.* **2016**, *16*, 57

Chapter 2: Into the nanoverse

2.1 Why so small?

In the previous chapter we discussed the push for miniaturization of transistors to improve efficiency/power density. These advances were all contingent on nanoscience, a growing field with applications far beyond information transfer and storage. Nanomaterials have unique properties from their bulk that make them especially attractive topics of research. One example is the massive surface area that they can offer, which is frequently exploited in battery technology as it allows for increased intercalation rates and more complete charging. We use these same principles to optimize our magnetoionic-like device, as will be seen in Chapter 4.

2.2 Magnetism at the nanoscale

Owing to their tunability and versatility in a broad spectrum of applications, magnetic nanoparticles (MNPs) have been a central focus in nanoscience research. Many of these applications lie in the field of biomedicine, where MNPs are under study for targeted drug delivery in cancer treatment, biosensing, magnetic resonance imaging (MRI), and hypothermia treatment.[1] These useful nanocrystals are also employed in magnetic separation and water purification.[2,3] Furthermore, MNPs hold great promise in nanoelectronics, spintronics, and high-density computer memory storage with improved efficiency.[4]

Many of these applications are contingent on the particle's superparamagnetic behavior. Superparamagnetism (SPM) is an exclusively nanoscale phenomenon occurring in sufficiently small single-domain particles.[5] This behavior arises when the magnetocrystalline anisotropy energy falls below the system's thermal energy, $k_B T$, allowing for the spontaneous switching of the magnetic domain direction, with the result being a time-averaged net magnetization of zero. SPM is favorable in many applications because these magnetic moments will align with external fields, like a paramagnet but with much higher magnetic saturation. The lack of net magnetism also allows for

easy particle suspension without agglomeration. Furthermore, SPM is exploitable in the construction of multiferroic on-off switchable magnets.[6] Due to the highly specific nature of SPM, synthetic methods must allow for control over the particle's anisotropy energy, which is dependent on several factors including particle size, shape, and surface.

2.3 Fabricating nanomaterials

Nanoparticle properties are highly dependent on their synthesis method, of which there are many. These synthetic approaches can be broadly grouped into two categories: top-down, where materials are created in bulk and then mechanically reduced to nanoscale; and bottom-up, where elemental precursors are coprecipitated into nanomaterials. While top-down approaches, such as ball milling, are affordable and excel at maintaining stoichiometric control for specific phases, they tend towards poor size and shape dispersity, and have long synthesis times.[7] As a result, the more sophisticated and tunable bottom-up approaches are more commonly employed in recent advances.

2.3.1 Solution-phase synthesis

Bottom-up synthesis methods exist in a wide variety, including ceramic solid-state routes, gas-phase condensation, reactions in oil emulsions, and solution-phase approaches.[8] Of these, solution-phase methods have been most widely employed due to the sophisticated molecular control allowed by their formation mechanisms.[9]

The formation mechanism of colloidal nanoparticles in solution is broadly explained by the 1950 theory of LaMer burst nucleation.[10] The first step in burst nucleation involves a steady increase in monomer concentration as the precursor dissolves until a critical supersaturation concentration is reached. At this point, many nuclei are formed in a short period of time, or burst, which decreases the monomer concentration to the equilibrium concentration, thereby ending the nucleation process. The nuclei then grow in a slower growth step, resulting in clearly defined stages of nucleation and growth. The thermodynamic and kinetic equations that govern classical nucleation

and growth theories are useful tools for researchers to guide their synthesis parameters for the desired nanoparticle properties. Generally, these modifications involve the reaction time, temperature, and precursor concentrations. Since the rates of nucleation and growth are highly dependent on the forming particle's surface energy, precise synthetic control can be further advanced by the addition of a surfactant to the formation reaction.[11]

Although nanoparticles synthesized via burst nucleation and growth mechanisms are highly tunable, these routes are not without limitations. One of the major drawbacks of mechanisms involving the rapid burst formation of nuclei is that smaller nanoparticles can be difficult to select for. This is due to the critical size requirement for nuclei stability before growth can begin. This condition will be further discussed in Chapter 3.

2.3.2 Tunability with surfactants

Solution phase synthesis can either be solvent-controlled or surfactant-assisted. In the more sophisticated surfactant-assisted synthesis, nanoparticle formation occurs in the presence of a surfactant that acts as a surface capping agent and a stabilizing ligand. This surfactant is usually a fatty acid comprised of a coordinating head and a long, nonpolar alkyl tail. During nanoparticle formation, the surfactant's coordinating head reversibly attaches to the particle surface, stabilizing the particle and mediating its growth. The surfactant also allows for extremely high size tunability and near monodispersity because nucleation rate depends on the new particle's surface free energy. Adding a surfactant can change the surface free energy, allowing for control over nucleation rate according to identity (binding affinity and alkyl tail length/size) and the concentration of surface capping ligand.[11] Another benefit of surfactant-assisted synthesis is that the steric interactions between the long surfactant alkyl groups prevent particles from agglomerating.[12] Surfactants can be exchanged following particle formation, allowing researchers to tailor surface activity post-synthesis.

Finally, the surfactant forms a micelle-like structure around the nanoparticle, allowing it to be easily suspended in an apolar solvent after synthesis.

2.4 References

(1) McNamara, K.; Tofail, S. A. *Adv. Phys.* **2016**, *2*, 54–88.

(2) Yildiz, I. *Nanotechnol. Rev.* **2016**, *5*, 331-340.

(3) Martinez-Boubeta, C.; Simeonidis, K. *Micro Nano Tech.* **2019**, 521-552.

(4) Chiolerio, A.; Allia, P. Encyclopedia of Nanotechnology. *Springer, Dordrecht.* **2012**, 1248-1256.

(5) Kudr, J.; Haddad, Y.; Richtera, L.; Heger, Z.; Cernak, M.; Adam, V.; Zitka, O. *Nanomaterials* **2017**, *7*, 9.

(6) Kim, H. K.; Schelhas, L. T.; Keller, S.; Hockel, J. L.; Tolbert, S. H.; Carman, G. P. *Nano Lett.* **2013**, *13*, 884–888.

(7) Hadef, F. *Powder Technology* **2017**, *311*, 556–578.

(8) Rao, C. N.; Müller, A.; Cheetham, A. K. Nanomaterials Chemistry *Wiley-VCH, Weinheim*, **2007**.

(9) Cushing, B. L.; Kolesnichenko, V. L.; O'Connor, C. J.. *Chem. Rev.* **2004**, *104*, 3893-3946.

(10) LaMer, V. K.; Dinegar, R. H. *J. Am. Chem. Soc.* **1950**, *72*, 4847-4854.

(11) X. Jia, *et al. J. Phys. Chem. C.* **2008**, *112*, 911–917.

(12) Shaban, S. M.; Kang, J.; Kim, D. H. *Compos. Commun.* **2020**, *22*, 100537

Chapter 3: Low polydispersity, scalable synthesis of cobalt ferrite nanoparticles via continuous solvothermal growth

3.1 Introduction

In chapters one and two, we introduced the importance of establishing voltage control of magnetism and discuss the uniquely useful properties of nanomaterials as well as some of their fabrication methods. In this chapter, we report the optimization of a novel cobalt iron oxide nanoparticle synthesis technique for the development of a strain-mediated multiferroic composite.

3.1.1. Why CFO?

Nanoscale cobalt iron oxide, or cobalt ferrite (CFO), is an exceptionally useful material. This inverse spinel structure is made up of face-centered cubic oxygen anions with Fe^{3+} ions in the tetrahedral sites and both Co^{2+} and Fe^{3+} ions in the octahedral sites.[1] Like other ferrites, CFO finds wide utility in sensing, catalysis, drug delivery, and magnetic memory storage.[2,3] Within these applications, CFO excels above other ferrites due to its chemical and mechanical stability, allowing for its use in a variety of environments, particularly in vivo.[4] Cobalt ferrite is also favorable due to its affordability, low electrical conductivity, high Curie temperature, and large magnetostrictive response. Finally, CFO has a substantial magnetocrystalline anisotropy, surpassing that of ferrite tenfold, which can be synthetically tuned by varying stoichiometric iron and cobalt ratios.[5] These characteristics make CFO a particularly good candidate for radio-frequency hypothermia heat treatment and magnetic imaging.

3.1.2 Common CFO synthesis methods

The wide potential of CFO has led researchers to develop a variety of synthesis methods to efficiently and easily produce nanoparticles with the desired properties. Generally, the formation of metal oxide nanoparticles depends on the transformation of a metal-containing precursor species into an oxidic compound containing metal-oxygen bonds. The oxygen source broadly separates the

different synthetic approaches. In liquid-phase approaches, nonaqueous routes offer a control-advantage over aqueous methods because carbon-oxygen bonds act as less reactive oxygen sources than water.[6] The lower reactivity in nonaqueous solutions slows growth and yields more monodisperse products. Therefore, most efforts to synthesize CFO have involved solvothermal techniques in which metal precursors are dissolved in a solvent and heated. These methods often make use of surfactants to further mediate particle growth. However, even this degree of control can be insufficient to precisely achieve particles with certain parameters.

3.1.3 A new chapter in nanoparticle synthesis

As discuss in Section 2.3.1, synthetic tuning of physical nanoparticle properties, particularly of size, can be difficult using conventional La Mer-type mechanisms due to the rapid burst nucleation event. For this reason, some recent work has sought to turn away from mechanisms with distinct nucleation and growth steps, and toward more controlled synthesis routes. Among these is a continuous growth process of ferrite nanoparticles outlined by Chang et al.[7] This novel method involves the dissolution of metal salt precursors with oleic acid at low temperature to form an iron-oxo-oleate complex. Upon addition of 1-decanol at higher temperatures (100-180 ºC), this complex undergoes an esterification reaction that removes the strongly binding oleate ligands to form hydroxyl-activated metal centers and decyl-oleate side products. These centers can then combine and grow into larger particles by hydroxyl group condensation between metal cores. The result is a controlled and continuous growth in nanoparticle size due to the strongly binding ligands reducing the formation energy of increasingly large iron-oxo clusters.

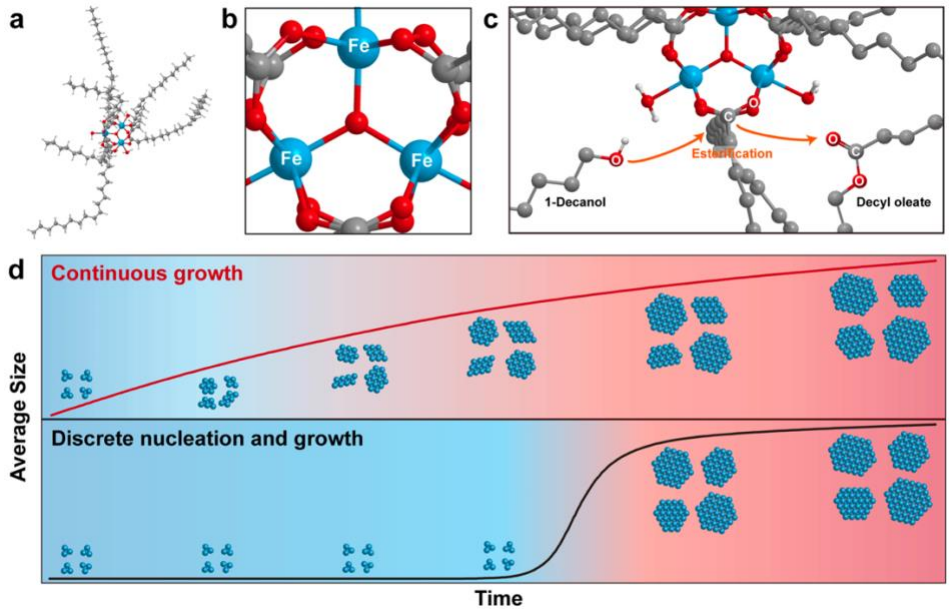

Figure 3.1. Shows the structures and mechanisms involved in Chang et al.'s continuous iron oxide nanoparticle growth model. A tri-oxo-core (b) is bound by oleate ligands to form an iron oleate cluster. The ligands are then removed by decanol (c), presumably giving the cluster an opportunity to grow following the continuous growth scheme rather than the nearly universal practices of burst nucleation and growth (d). Reprinted from Chang, H.; Hyo Kim, B.; Young Jeong, H.; Hee Moon, J.; Park, M.; Shin, K.; In Chae, S.; Lee, J.; Kang, T.; Kyu Choi, B.; Yang, J.; Bootharaju, M. S.; Song, H.; Hee An, S.; Man Park, K.; Yeon Oh, J.; Lee, H.; Soo Kim, M.; Park, J.; Hyeon, T. *J. Am. Chem. Soc.* **2019**, *141*, 7037-7045 with permission from the American Chemical Society.

Herein, a novel CFO synthesis method is developed following the methodology put forth by Chang et al. for the synthesis of iron oxide nanoparticles. This method, in which metal-oxo-oleate complexes undergo esterification with a primary alcohol to produce the desired nanoparticles, follows a continuous growth mechanism and does not proceed via a burst nucleation step. We demonstrate that the implementation of the continuous growth mechanism allows for more precise control of CFO nanoparticles in the extremely small range of 3-8 nm, simply by varying reaction time and temperature. Furthermore, we show that this straightforward technique is scalable and that its resulting particles offer much greater monodispersity than those fabricated via conventional solvothermal methods.

3.2 Experimental

3.2.1 Literature conventional synthesis of CFO nanoparticles

All nanoparticles following the classical solvothermal synthesis were synthesized as modified from Lu et al. In a 50 mL Schlenk flask, 63.0 mg cobalt (II) acetylacetonate (0.245 mmol, Aldrich, 97%), 125 mg Iron (III) acetylacetonate (0.354 mmol, Aldrich, 99.9%), and 155 mg 1,2-hexadecandiol (0.600 mmol, Aldrich, 90%) were dissolved with a magnetic stir bar in a mixture of 6 mL oleylamine (Panreac, purified by distillation), 2 mL oleic acid (Panreac, purified by distillation), and 4 mL n-octyl ether (Aldrich, 99%). After being degassed at RT for 10 minutes, the solution was dried under vacuum at 100 ºC for 30 minutes. Under argon, the mixture was heated to 250 ºC in a 15-minute ramp period and held for 30 minutes. The resulting nanoparticles were cooled to RT, centrifuged, decanted and dispersed in hexanes before being washed with ethanol twice and re-dispersed in hexanes.

3.2.2 Synthesis of cobalt-iron-oxo-oleate complex

Cobalt-iron-oxo-oleate complexes were formed in a 50 mL Schlenk flask by dissolving 50 mg cobalt (II) acetylacetonate (0.194 mmol, Aldrich, 97%) and 141 mg Iron (III) acetylacetonate (0.399 mmol, Aldrich, 99.9%) with a magnetic stir bar in a mixture of 5 mL oleic acid (15.75 mmol, Panreac, purified by distillation) and 6 mL n-octyl ether (19.95 mmol, Aldrich, 99%). After being degassed at RT for 10 minutes, the solution was dried under vacuum at 100 ºC for 30 minutes.

3.2.3 Continuous esterification synthesis of CFO nanoparticles

While maintaining 100 ºC, 4 mL 1-decanol (20.95 mmol, 'Baker', 99%) was added to the flask containing the cobalt-iron-oleate complex under argon. The solution was heated to reaction temperature (180 or 200 ºC) in a 15-minute ramp period and held for a reaction time (30-600 minutes). The resulting nanoparticles were cooled to RT, centrifuged, decanted and dispersed in hexanes before being washed with ethanol twice and re-dispersed in hexanes.

3.2.4 Instrumentation

Transmission Electron Microscopy (TEM) images were collected using an FEI Tecnai T12 quick room temperature microscope. Magnetic measurements were conducted using a superconducting quantum interference device (SQUID) magnetometer (Quantum Design, MPMS XL-5). Oxidation potential of surfaces and samples were carried out using X-ray Photoelectron Spectroscopy (XPS) from a Kratos Axis Ultra DLD spectrometer with a monochromatic Al (Kα) radiation source. Scanning electron microscope (SEM) images were taken via JEOL JSM-6700F FE-SEM.

3.3 Results and discussion

3.3.1 Improved morphology

TEM images of nanoparticles produced via different synthesis methods reveal improved spherical morphology resulting from the esterification method, as seen in Figure 3.2.

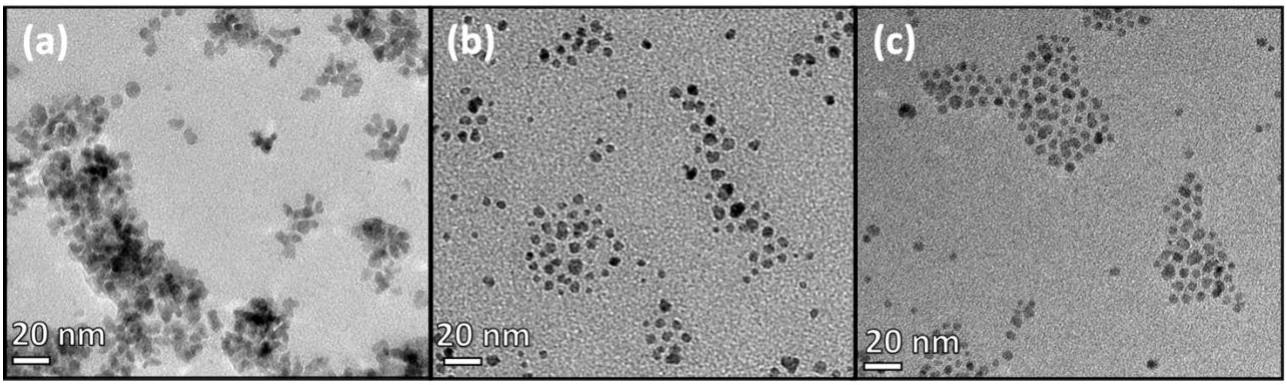

Figure 3.2. TEM Image of cobalt ferrite nanoparticles synthesized a) via the conventional method after 30-minute reaction at 250 °C, b) via the esterification method after 180-minute reaction at 180 °C, and c) via the esterification method after 180-minute reaction at 200 °C.

The particles produced via esterification (Figure 3.2.b-c) have more rounded and uniform edges than the jagged and irregular shapes formed by the conventional heat-up synthesis (Figure 3.2.a). The uniform spherical shape of the particles synthesized via esterification remains consistent across

different reaction temperatures. This is likely a result of the controlled removal of oleate binding ligands limiting the rate of growth and ensuring a more even ripening. Meanwhile, the rapid formation of particles in the conventional synthesis may result in a kinetic distribution across the particle, which causes it to grow unevenly. The particles formed via the conventional method also seem to suffer from agglomeration to a much greater extent than those synthesized via esterification.

3.3.2 Improved size distribution

Quantitative analysis of particle sizes from TEM images was carried out using ImageJ software. The results are presented in Figure 3.3. This data clearly demonstrates that the esterification synthesis route produces particle populations with a much lower polydispersity than those produced with the classical synthesis, for both one hour and three-hour reaction times.

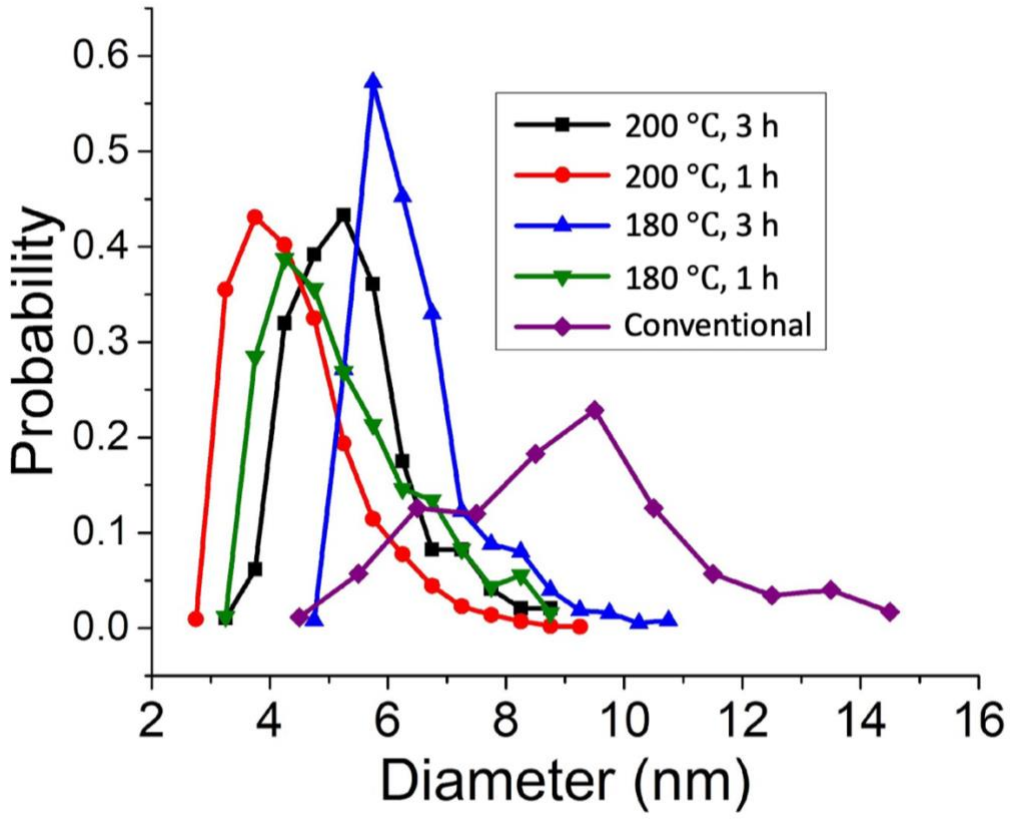

Figure 3.3. Size and size distribution of nanoparticles produced using 30-minute classical literature synthesis (purple), three-hour esterification synthesis at 200 ºC (black), one-hour esterification synthesis at 200 ºC (red), three-hour esterification synthesis at 180 ºC (blue), and one-hour esterification synthesis at 180 ºC (green).

Furthermore, a clear increase in particle sizes between one and three-hour esterification syntheses is observed as expected. It should also be noted that, despite the conventional particle distribution resulting from just a 30-minute reaction, these particles are much larger than those resulting from up to three hours of esterification. This highlights the difficulty in producing necessarily small nanoparticles with conventional heat-up methods, since very few nanoparticles are able to form during reactions lasting less than 30 minutes and those resulting from longer synthesis are inevitably much larger.

Another interesting observation that can be drawn from this figure is that the esterification syntheses carried out at lower temperatures result in larger nanoparticles on average than esterification reactions at higher temperatures. This trend, which is consistent at both one-hour and three-hour reaction times, will be further explored in Section 3.3.4.

3.3.3 Continuous growth confirmed by time-point analysis

A time point study of nanoparticle growth throughout the esterification synthesis was conducted by removing 1 mL reaction solution at various times during the reaction. These aliquots were dispersed in hexanes and washed with ethanol twice before being suspended in hexanes, as per usual procedure. The mean particle size at a given time point was determined by TEM and plotted for each reaction condition in Figure 3.4.

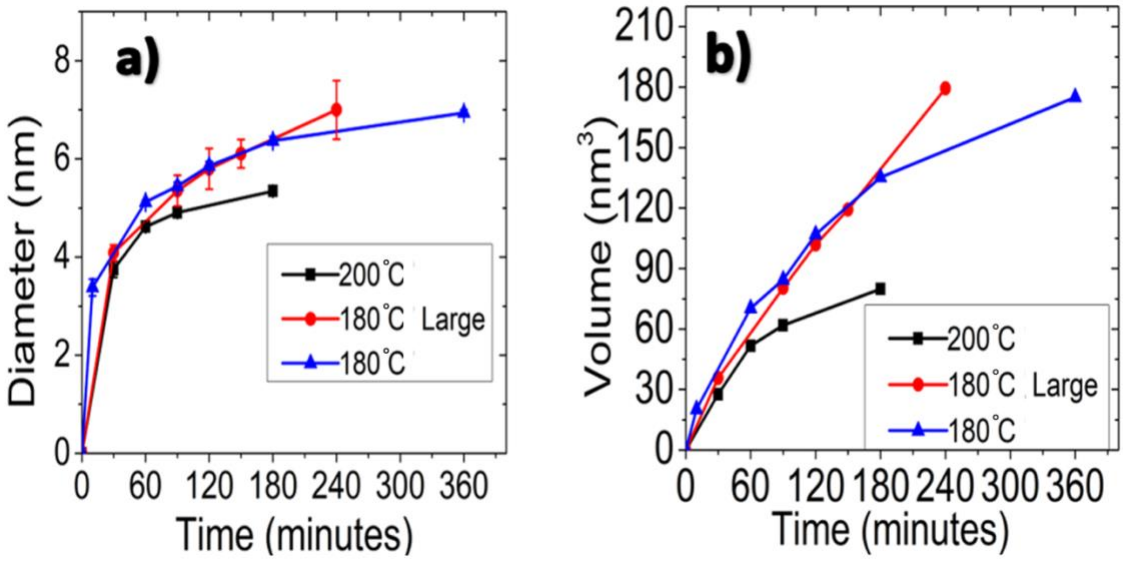

Figure 3.4. Time-point analysis of average CFO nanoparticle diameter through esterification syntheses of various scales and reaction temperatures as derived by TEM images. One mL aliquots were removed from the reaction solution throughout standard-scale syntheses at 180° C (blue) and 200° C (black), and throughout large-scale syntheses at 180° C (red). Average particle sizes were derived from each sample using TEM and ImageJ.

To demonstrate scalability, a larger esterification synthesis was carried out as described in Sections 3.2.2 and 3.2.3, but with all reagent amounts increased by a factor of four. The results indicate that both the standard and large-scale esterification syntheses result in particles whose diameter grow continuously at 180 °C, and whose volume increases linearly. This scalable behavior holds great promise for practical industrial application of this esterification method. However, while the particles initially appear to grow continuously at 200 °C, nanoparticle growth begins to slow after about the first hour. Although not explained, Chang et al. reported a similar reduction in continuous growth behavior in reactions carried out at higher temperatures. This suggests that the reaction proceeds via different mechanisms at different temperatures.

3.3.4 Elucidating alternate mechanisms at higher temperature

One alternative mechanism could be a La Mer-type rapid nucleation and growth, resulting from the spontaneous decomposition of metal-oxo precursor at higher temperatures like 200 °C. In

the event of some precursor thermal decomposition, a high concentration of metal ions could form in the solution, opening the possibility for a burst nucleation event to occur alongside the continuous growth. This would divert some of the starting material toward the formation of new nuclei, and away from the continuously growing particles, resulting in a smaller population average size than would be expected in a strictly continuous pathway. Chang et al. do report the thermal decomposition of the iron oxide trinuclear-oxo cluster at temperatures above 200 °C, as determined by thermogravimetric analysis (TGA). To explore this possibility in the cobalt ferrite system, precursors were added to solution and heated per the esterification synthesis method described in section 3.2.3, but without the addition of alcohol. No particles resulted from both 180 °C and 200 °C trials, which suggests that the precursors do not thermally decompose at 180 °C or 200 °C. It is likely that alcohol is required to catalyze precursor decomposition, even at high temperatures in the cobalt ferrite system.

Nanoparticle seeds have also been known to induce precursor decomposition, which can result in growth of the seeds and/or the formation of new nuclei in what is known as seed-mediated nucleation.[8] To test this possibility, CFO seeds were grown at 180 °C using the esterification method as described in Sections 3.2.2 and 3.2.3 with a 90-minute reaction time. The resulting seed crystals were isolated and reacted with metal-oxo precursors in oleic acid and n-octyl ether for 30 minutes as described in Section 3.2.3 but without the addition of alcohol. The results are presented in Figure 3.5.

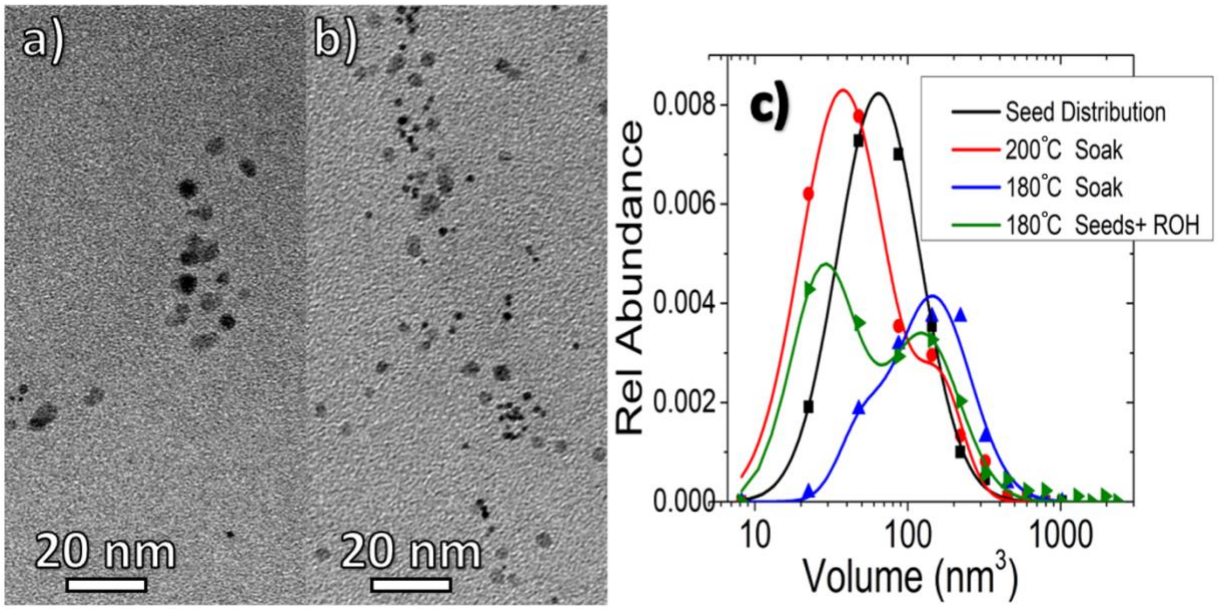

Figure 3.5. TEM images of CFO seeds after heating in a precursor solution absent of decanol for 30 minutes at a) 180 °C and b) 200 °C. c) Size distribution histograms acquired by ImageJ analysis of TEM images of CFO seeds before further reaction (black), and after heating in the absence of decanol at 180° C (blue) and 200° C (red) for 30 minutes. The change in distribution shows that metal-oxo precursor decomposition is possible at both 180 °C and 200 °C, but that it occurs more rapidly at 200 °C, allowing for the formation of new nuclei rather than prioritizing growth. c) Also shows the distribution of seeds grown at 180° C in a precursor solution *with* decanol (green), which confirms that new particle formation forms via esterification at 180° C.

Visual inspection of the TEM images reveals the formation of smaller nuclei at both 180° C and 200° C. While only a few new particles are apparent following reaction at 180° C, the majority of the imaged particles appear to be new nuclei following reaction at 200° C. Simultaneously, the seeds reacted at 180° C seem to have grown larger, while those at 200 °C remain quite small. These differences are quantified in a histogram in Figure 3.5.

Due to the changes in size distribution and mean size at both 180 °C and 200 °C, it is clear that seed-mediated decomposition of precursors is possible at both temperatures. However, the changes are very different at their respective temperatures. This may be a result of varied metal-oxo cluster decomposition rates at different temperatures. It should also be noted that, while the seed

distribution fits easily to one log normal curve, the particles resulting from seed-mediated synthesis at both 180° C and 200° C require two log normal curves to fit their distribution. This provides further evidence that two growth mechanisms are occurring simultaneously, one that primarily results in the formation of new nuclei, and another that supports the growth of pre-existing particles.

The relative peak sizes of the two size distributions are significantly different following reaction at 180 °C and 200 °C. At 180 °C the larger peak at 7.7 nm makes up approximately 80% of the total distribution while the smaller peak at 4.8 nm comprises only 20% of the total particle population. However, at 200 °C, an opposite trend is observed where the larger peak at 7.2 nm makes up only 30% of the total distribution, while the peak at 5.1 nm accounts for more than twice as much of the population. This suggests that at 180 °C, the precursors decompose more slowly, causing these components to contribute to further growth of the existing seeds since they do not provide enough material for forming nuclei to reach the critical stabilization size. Meanwhile, at 200 °C, the precursors decompose quickly, providing sufficient material to reach the critical concentration for a rapid burst of nuclei to occur, perhaps via a LaMer-type mechanism.

In a final experiment, a sample of seed crystals were heated at 180 °C for 30 minutes in a precursor solution *with* decanol. The size distribution of the resulting particles is recorded in Figure 3.5 (green). As with the previous particles grown from seeds, this histogram was necessarily fit with two peaks, indicating that two different size groups are resulting from this method. However, unlike the results from the same procedure carried out *without* decanol (blue), the smaller sized particles that averaged about 4.3 nm in diameter, were more abundant than the particles that grew larger to an average of 7.2 nm. This is the opposite of what was observed when decanol was omitted under the same conditions. This shows that decanol plays a key role, not only in facilitating the dissolution of

precursors into solution, but in initiating nucleation at temperatures lower than those typically used in solvothermal nanoparticle synthesis methods.

3.4 Conclusion

The Chang et al. esterification synthesis method for the continuous growth of iron oxide nanoparticles has been proven to be adaptable for CFO nanoparticles. The particles produced via this method were found to have far superior size and shape uniformity when compared to particles synthesized by a widely used solvothermal method. We also show that this cost effective and straightforward route is linearly scalable at least up to 0.8 mmol of product.

The thermodynamics of continuous CFO growth was further investigated to confirm that the esterification mechanism dominates nanoparticle formation at temperatures of 180 °C and below. However, La Mer burst nucleation begins to compete with esterification at higher temperatures.

The unique avoidance of a La Mer burst nucleation event in this procedure allows for precise control over nanoparticle size, even at extremely small regimes, by simple modifications in reaction temperature and/or time. This is a necessary development toward achieving efficient voltage control of magnetism and strain-mediated multiferroic composites.

3.5 References

(1) Kudr, J.; Haddad, Y.; Richtera, L.; Heger, Z.; Cernak, M.; Adam, V.; Zitka, O. *Nanomaterials* **2017**, *7,* 9.

(2) Lodeiro, C.; Roig, A.; Saccardo, P.; Bronstein, L. M.; Price, P. M.; Mahmoud, W. E.; Al-Ghamdi, A. A. *www.frontiersin.org* **2018** *6*, 619.

(3) Harada, M.; Kuwa, M.; Sato, R.; Teranishi, T.; Takahashi, M.; Maenosono, S. *ACS Appl. Nano Mater.* **2020**, *2020*, 8389–8402.

(5) Reddy, L. H.; Arias, J. L.; Nicolas, J.; Couvreur, P. *Chem. Rev.* **2012**, *112*, 11.

(6) Niederberger, M.; Pinna, N. Metal Oxide Nanoparticles in Organic Solvents. *Springer-Verlag*, New York, **2009**.

(7) Chang, H.; Hyo Kim, B.; Young Jeong, H.; Hee Moon, J.; Park, M.; Shin, K.; In Chae, S.; Lee, J.; Kang, T.; Kyu Choi, B.; Yang, J.; Bootharaju, M. S.; Song, H.; Hee An, S.; Man Park, K.; Yeon Oh, J.; Lee, H.; Soo Kim, M.; Park, J.; Hyeon, T. *J. Am. Chem. Soc.* **2019**, *141*, 7037-7045

(8) Lu, A. H.; Salabas, E. L.; Schüth, F. *Angew. Chem. Int. Ed.* **2007**, *46*, 1222–1244.

Chapter 4: Magnetic control of Sm-Co alloys via electrochemical hydrogen charging

4.1 Introduction

As described in chapter 1, magnetoionics offer a highly promising method for magnetic modulation in metals in which ions are intercalated into the magnetic material's crystal lattice, where they undergo faradaic reactions. However, this route to the voltage-control of magnetism has three major drawbacks. First, due to the high electric-field screening in the metal, the charged ion migration, and thus the depth of magnetic manipulation, is limited to the few atomic layers nearest the ion-source material.[1,2] Second, the magnetic material is prone to degradation as a result of the ion intercalation and electrochemical reactions[3]. Similarly to the erosion effect observed in battery electrode materials, the decomposition of the magnet crystal lattice creates a challenge for reversibility and shortens device lifetime. Finally, the change in coercivity induced in magnetoionics is yet too weak for practical application.[4]

4.2 Magnetic control via hydrogen charging

These shortcomings can all be improved by opting to exchange ions for a neutral species. Hydrogen is an excellent choice because it is very small, abundant, and cost effective. Although this method also relies on intercalation, the working principle of magnetic control via hydrogen charging varies from magnetoionics in that the magnetic change results from lattice expansion or distortion rather than from electrochemical conversion-type reactions.[5,6]

Most past efforts to control magnetism using hydrogen have employed the gas-phase under elevated pressures.[7] While this has been shown to induce incredibly large changes in magnetism, the use of high pressures is not practical in small-scale devices. Furthermore, hydrogen discharging via this method is very slow unless facilitated by elevated temperatures, which also are not practical for electronic applications. Therefore, recent work has sought alternate routes to hydrogen charging, leading to the discovery that the same effect can be accomplished electrochemically via an aqueous

electrolyte.[5] Electrochemical hydrogen charging opens possibilities to induce large modulations in magnetic properties simply by applying a small voltage.

In both mechanism by which hydrogen is absorbed into the metal crystal lattice begins with the adsorption of a hydrogen-containing species to the metal surface.[5,8] In the case of gas-phase hydrogenation, this adsorbate is H_2 gas, while water is the adsorbed species in electrochemical routes. In the former, the metal catalyzes the dissociation of hydrogen gas into hydrogen atoms, which then diffuse into the crystal lattice driven by the concentration gradient of hydrogen atoms accumulated on the surface. Electrochemically, the water is reduced into hydroxide anions that return to the electrolyte and hydrogen atoms that proceed to migrate into the crystal lattice driven by the gradient. When hydrogen pressure is removed (gas-phase discharging), hydrogen atoms near the metal surface recombine into hydrogen gas, which leaves the material surface. Driven by the resulting gradient, hydrogen atoms from within the lattice migrate toward the surface where they too recombine into hydrogen gas. In electrochemical hydrogen discharging, the hydrogen atoms near the metal surface are oxidized and recombined with hydroxide ions in the electrolyte. Internal hydrogen atoms then move out to the surface, where they meet the same fate. The electrochemical hydrogen charging mechanism of the magnetic metal alloy, $SmCo_5$, is visualized in Figure 4.1.[5]

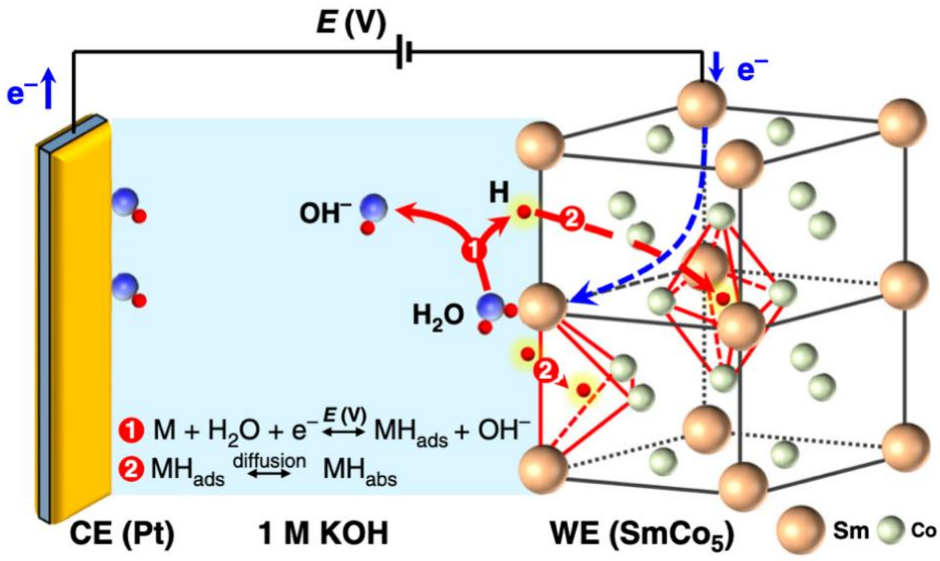

Figure 4.1. Schematic showing the mechanism of $SmCo_5$ electrochemical hydrogen charging under basic conditions. Reprinted from Ye, X.; Singh, H.K.; Zhang, H. *et al.* Giant voltage-induced modification of magnetism in micron-scale ferromagnetic metals by hydrogen charging. *Nat. Commun.* **2020**, *11*, 4849. Under creative commons http://creativecommons.org/licenses/by/4.0/.

4.3 The Sm-Co system

$SmCo_5$ and Sm_2Co_{17} have recently garnered interest for use in this application, as they both have large magnetization and high hydrogen storage capacity.[9,10] These alloys also have large magnetocrystalline anisotropies and exceptionally high Curie temperatures, making them more stable from thermal agitation, even in nanoscale devices, than their competitors. Furthermore, Sm-Co alloys are widely appreciated for their great resistance to corrosion, which is essential for their use in electrochemical hydrogen charging since highly alkaline electrolytes are necessary. Finally, the electrochemical potential equivalent to the equilibrium hydrogen pressures of these Sm-Co alloys is easily accessible and near the standard electrolysis potential of water.[11]

4.3.1 Structural properties

While $SmCo_5$ and Sm_2Co_{17} share many similarities, their magnetic properties and hydrogenation physics are very different. An investigation and comparison of these two alloys for

the voltage control of magnetism via electrochemical hydrogen charging can provide further insight into the various properties, conditions, and mechanisms that give way to useful and efficient devices. What follows for the remainder of this introduction is a more in-depth review of these materials.

$SmCo_5$ and Sm_2Co_{17} are both equilibrium phases in the Sm-Co system and have related structures.[12] $SmCo_5$ exists only in a hexagonal $CaCu_5$-type structure (*P6/mmm* space group) and has six atoms per unit cell. The more cobalt-rich Sm_2Co_{17} has a temperature-dependent crystal structure that is rhombohedral Th_2Zn_{17}-type ($R\bar{3}m$) below 1300 °C and hexagonal Th_2Ni_{17}-type ($P6_3mmc$) at higher temperatures. For the remainder of this thesis, we will only consider the rhombohedral structure since all experiments were carried out well below this temperature threshold. Although the rhombohedral Sm_2Co_{17} has a much larger unit cell of 38 atoms, this structure can be derived from the hexagonal $SmCo_5$ by substituting one third of samarium atoms with a dumbbell of cobalt atoms.

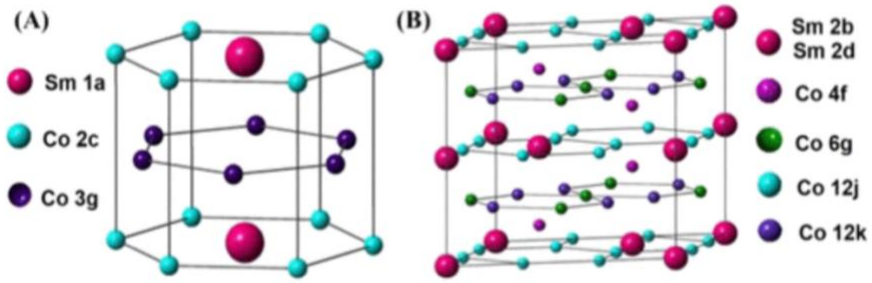

Figure 4.2 Crystal structures of $SmCo_5$ (A) and Sm_2Co_{17} (B). Reprinted from Ma, Z.; Mohapatra, J.; Wei, K.; *et al.* Magnetic nanoparticles: synthesis, anisotropy, and applications. *Chem. Rev.* **2021** with permission from the American Chemical Society.

4.3.2 Magnetic properties

A material's overall magnetism is dictated by both intrinsic and extrinsic properties. Intrinsic magnetism arises from quantum mechanical interactions at the atomic scale and is entirely unaffected by larger scale characteristics such as mictrostructure, which are important for extrinsic

magnetic properties. Generally, intrinsic magnetism can be understood by looking at the exchange coupling between the magnetic moments of electrons in different orbitals.

$SmCo_5$ has excellent intrinsic magnetic properties. Mainly, $SmCo_5$ has an exceptionally high uniaxial magnetocrystalline anisotropy with an easy axis that passes parallel to the hexagonal planes.[13] This anisotropy, that results from the single-ion anisotropy of Sm^{3+}, is the reason for the alloy's high coercivity.

Sm_2Co_{17}, while still possessing favorable intrinsic magnetic properties, does not have a coercivity to match that of $SmCo_5$.[14] This is because many of the Sm atoms in $SmCo_5$ have been substituted for Co atoms in Sm_2Co_{17}, resulting in fewer of the strong Sm-Co exchange interactions are responsible for the huge anisotropy in $SmCo_5$. Instead Sm_2Co_{17} has an easy plane anisotropy that is parallel to the basal plane. Some intrinsic magnetic properties of $SmCo_5$ and Sm_2Co_{17} are provided in Table 4.1.[15]

Table 4.1. Intrinsic magnetic properties of $SmCo_5$ and r-Sm_2Co_{17}. T_c is Curie temperature, M_S is magnetization saturation, and K_1 is the anisotropy constant.

	T_c (K)	M_S (MA m^{-1})	K_1 (MJ m^{-3})
$SmCo_5$	1020	0.86	17.2
r-Sm_2Co_{17}	1190	0.97	4.2

Much research has gone into tailoring magnetic alloys to achieve the best possible magnetic properties. Both intrinsic and extrinsic magnetic properties can be targeted using various sintering/processing techniques and by varying alloying conditions such as temperature, heating and cooling rates, pressure. Magnetism can also be improved by adding small stoichiometric amounts of other transition metals. One particularly successful example of this is seen in Sm_2Co_{17} magnets

doped with a blend of Fe, Cu, and Zn. In fact, these so called Sm_2Co_{17}– type pinning magnets have such exceptional magnetic properties that the use of this magnet far exceeds the use of pure Sm_2Co_{17}.[16,17]

The Sm_2Co_{17}-type system is highly complex, but the overall intercellular structure can be described as follows.[18] The majority of the structure consists of Fe-rich Sm_2Co_{17} grains. The iron replaces some of the cobalt in the Sm_2Co_{17} phase and serves to increase the saturation magnetization. These grains are divided by Cu-rich $SmCo_5$ where copper increases the domain wall energy of the cell boundaries, thereby increasing coercivity. The entire cellular structure is traversed by a zirconium lamellar phase, or Z-phase, which is believed to further enhance coercivity by providing additional pinning sites, but this to a much lesser degree than the $SmCo_5$ boundaries.

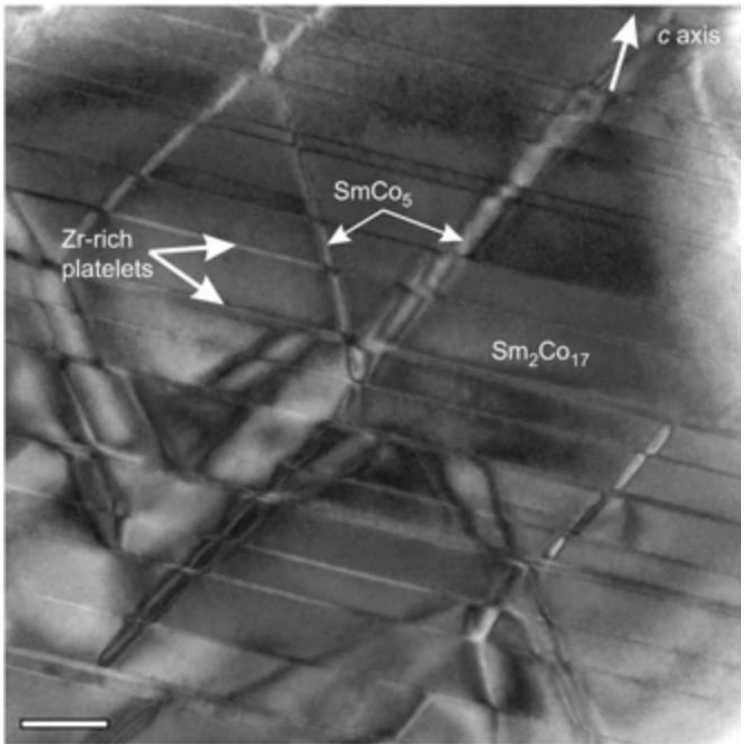

Figure 4.3. Bright-field TEM image of a Sm_2Co_{17}-type magnet. Reprinted from Duerrschnabel, M.; Yi, M.; Uestuener, K.; Liesegang, M.; Katter, M.; Kleede, H.-J.; Xu, B.; Gutfleisch, O.; Molina-Luna, L. Atomic structure and domain wall pinning in samarium-cobalt based permanent magnets. *Nat. Commun*. **2017**, *8*, 54. under creative commons http://creativecommons.org/licenses/by/4.0/.

4.3.3 Hydrogenation behavior

In addition to Sm-Co alloys having varied magnetic and structural properties in different stoichiometries, they also form hydrides with different kinetics and thermodynamics. One of the main methods of analyzing a material's hydrogenation capacity is to collect a pressure-composition-temperature (P-C-T) curve. These plots apply an increasing hydrogen pressure and measure the resulting absorbed hydrogen concentration at a constant temperature. This process is repeated to collect hydrogen content vs hydrogen pressure curves at different temperatures.

The first slope of a P-C-T curve indicates the stage where the storage material forms a solid solution with some dissolved hydrogen, this is called the "α-phase".[19] The start of a pressure plateau, if there is one, indicates that an ordered hydride "β-phase" has begun to grow. The β-phase will continue to grow up until the end of the plateau, when all the metal has formed a hydride. This plateau pressure is also known as the equilibrium hydrogen pressure. Figure 4.4 Shows a P-C-T curve for $LaNi_5$, another hexagonal RT_5 hydrogen storage material.[19]

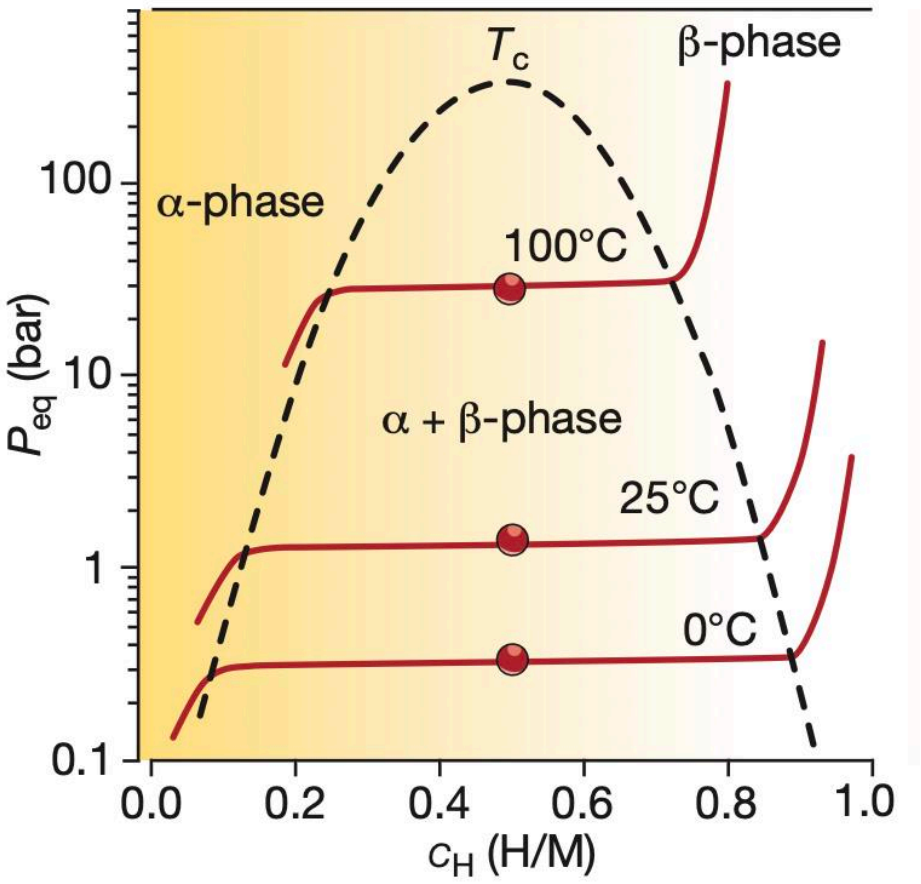

Figure 4.4. Pressure-composition-temperature curve of $LaNi_5$. Reprinted from Schlapbach, L.; Züttel, A. Hydrogen storage materials for mobile applications. *Nature*. **2001**, *414*, 353-358 with permission from Springer Nature.

The P-C-T curve of $SmCo_5$ closely resembles that of $LaNi_5$ in Figure 4.4, with approximate equilibrium pressures of 10 atm at 40 °C, 19 atm at 60 °C, and 35 atm at 80 °C.[20] Multiple reports have shown that $SmCo_5$ forms a hydride with approximately 2.6 hydrogen atoms, which is the equivalent of 0.43 H/M, at an equilibrium pressure of 4 atm at room temperature.[21] The hydrogenation of $SmCo_5$ to form $SmCo_5H_{2.6}$ induces an anisotropic deformation of the crystal lattice from a hexagonal structure to a body-centered orthorhombic one.

The phase transition from the hexagonal $SmCo_5$ to the orthorhombic $SmCo_5H_{2.6}$ can be clearly observed through x-ray diffraction. The most tracible change is notably the splitting of the hexagonal 110 peak into orthorhombic 020 and 103 peaks.[5]

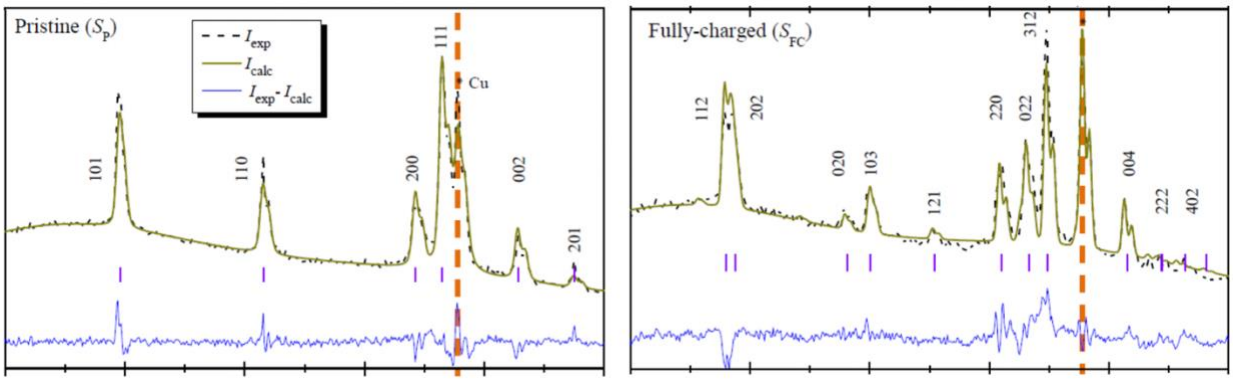

Figure 4.5. Powder X-ray Diffraction of pristine (a) and fully hydrogen charged (b) $SmCo_5$. Reprinted from Ye, X.; Singh, H.K.; Zhang, H. *et al.* Giant voltage-induced modification of magnetism in micron-scale ferromagnetic metals by hydrogen charging. *Nat. Commun.* **2020**, *11*, 4849. Under creative commons http://creativecommons.org/licenses/by/4.0/.

Meanwhile, hydrogenation of single-phase rhombohedral Sm_2Co_{17} results in a uniform expansion of the basal plane.[22] While Sm_2Co_{17} can absorb up to 0.3 H/M at pressures of 60 atm or above, it only takes up ~0.16 H/M with 4 atm of pressure at 150 °C. Furthermore, due to the slow hydriding kinetics of this compound, gas-phase hydrogenation has not been observed below 150 °C, even after 48 hours of high-pressure exposure.

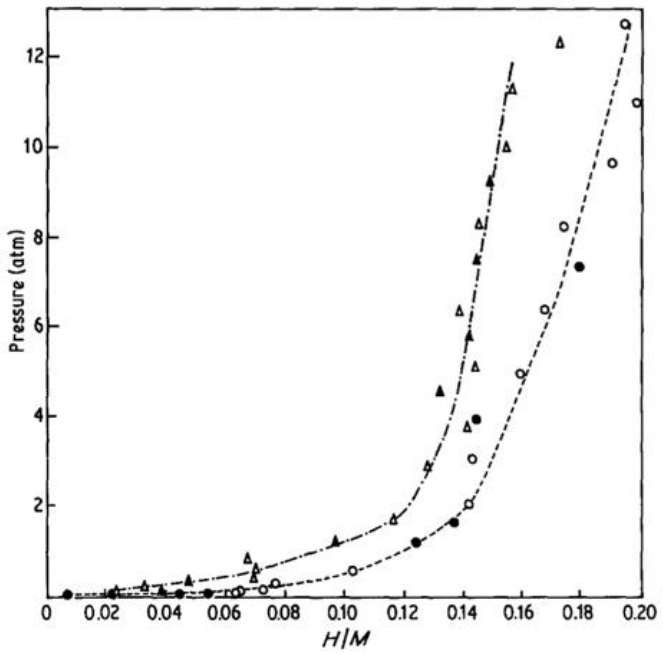

Figure 1 P–C–T data for Sm_2Co_{17}. 150° C Isotherm; ○ adsorption, ● desorption. 200° C Isotherm; △ adsorption, ▲ desorption. ⊢⊣ Typical error in *H/M*.

Figure 4.6. Pressure-composition-temperature curve of Sm_2Co_{17}. Reprinted from Evans, J.; King, C. E.; Harris, I. R. The hydrogenation behavior of the phases Sm_2Co_{17} and Pr_2Co_{17}. *J. Mater. Sci.* **1985**, *20*, 817-820 with permission from Springer Nature.

Finally, it should be noted that although the hydrogenation capabilities of doped Sm_2Co_{17}-type magnets have not been well-investigated, some findings suggest that the increase in cell and grain boundaries as compared to single-phase Sm_2Co_{17}, create channels through which hydrogen atoms can migrate, allowing for faster hydrogenation kinetics.[6]

4.4 Experimental

4.4.1 Materials

Fine $SmCo_5$ powder was purchased from Alfa Aesar (Stock no. 42732). The 30-mesh powder was analyzed using powder X-ray diffraction (Panalytical with Cu K_α source) and scanning electron microscopy (JEOL JSM-6700F FE-SEM) with energy dispersive spectroscopy, which confirmed the received material was $SmCo_5$. The Sm_2Co_{17} ingots were purchased as $SmCo_5$ from Sigma Aldrich (Stock no. 692859), however X-ray diffraction revealed that the received material was not $SmCo_5$,

but Sm_2Co_{17}. The ingot was used whole in electrochemical measurements but was mechanically ground with a mortar and pestle in an air-free environment for analysis and gas-phase hydrogenation experiments.

4.4.2 Slurry preparation

Slurries were prepared using as-received $SmCo_5$ that was vibration ball-milled for 1 h. The resulting powder was mixed with a 5% PVDF in NMP solution in a 10:90 ratio of binder to active material. Slurries were then cast onto copper foil with a doctor blade to a thickness of 15 μm. After drying under ambient conditions for 1 h, the slurries were vacuum dried at 80 °C overnight.

4.4.3 Electrochemical set-up

The $SmCo_5$ slurries and as-received Sm_2Co_{17} ingots were electrochemically charged and discharged with hydrogen using a three-electrode set up with a potentiostat (BioLogic VSP). A piece of platinized silica was used as the counter electrode with a Hg/HgO (1 M KOH) reference electrode. The cell was completed with an ultrapure 1 M KOH electrolyte.

4.4.4 Gas-phase hydrogenation

As-received $SmCo_5$ powder was placed into a 50 mL two-neck flask. The flask was evacuated for an hour before being exposed to a positive pressure of pure hydrogen gas by securing a hydrogen-filled balloon to one of the flask noses and leaving at room temperature for 30 hours.

Pieces of the Sm_2Co_{17} ingot were ground into a powder using a mortar and pestle in an air-free environment. The resulting particles were placed on a Si sample holder and heated in a quartz tube furnace at 150 °C for 30 hours while flowing pure hydrogen gas.

Both 'hydrogenated' materials were placed into a bath of liquid nitrogen prior to removing the hydrogen gas source. These samples were immediately analyzed using PXRD. To eliminate misleading peak shifts due to changes in sample height, the sample and sample holder were left untouched throughout the entire data collection. The results are discuss in 4.5.2.

4.4.5 Instrumentation

All powder X-ray diffraction patterns were collected using a Panalytical X'Pert Pro with a Cu K_α source in reflection geometry. Magnetic measurements were conducted using a superconducting quantum interference device (SQUID) magnetometer (Quantum Design, MPMS XL-5). X-ray photoelectron spectroscopy (XPS) was carried out with a Kratos Axis.

4.5 Results and discussion

4.5.1 Electrochemistry

This work was largely inspired by previous reports of giant voltage-induced modification of coercivity in $SmCo_5$. With the ultimate goal of further enhancing this magnetic control, we seek to develop similar methodologies with nano- rather than micron-scale Sm-Co. The increased surface area provided by nanomaterials should increase the extent and rate of hydrogenation. The latter will allow for faster magnetic switching, which would alleviate a crucial barrier currently preventing the implementation of this technology.

In pursuit of this aim, we must first establish that the reported observations can be replicated. Figure is the CV curve collected by Ye et al.[5] for the electrochemical hydrogenation of $SmCo_5$. The reducing peak around -0.9 V vs Hg/Hgo signifies the adsorption of hydrogen atoms onto the $SmCo_5$ electrode surface. The more reducing peak around -1.2 V results from the absorption of these hydrogen atoms into the $SmCo_5$ crystal lattice, as well as the start of some water splitting. The returning oxidizing peak corresponds to the subsequent desorption of hydrogen from their $SmCo_5$ electrode.

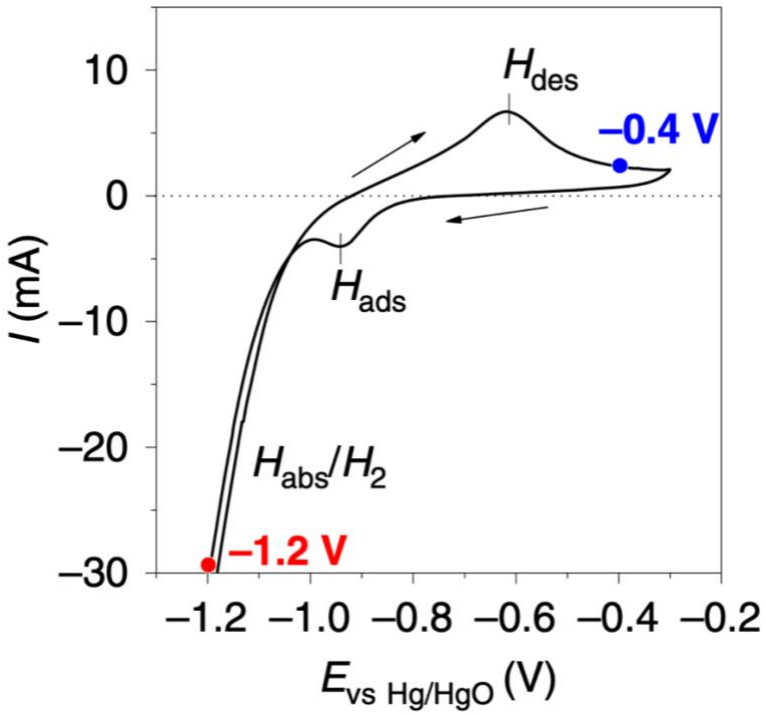

Figure 4.7. Cyclic voltammogram showing hydrogen adsorption, absorption, water splitting, and hydrogen desorption from an $SmCo_5$ electrode in 1 M KOH with a Pt wire counter electrode and Hg/Hgo reference. Reprinted from Ye, X.; Singh, H.K.; Zhang, H. *et al.* Giant voltage-induced modification of magnetism in micron-scale ferromagnetic metals by hydrogen charging. *Nat. Commun.* **2020**, *11*, 4849. Under creative commons http://creativecommons.org/licenses/by/4.0/.

Many Sm-Co electrodes were fabricated using as-purchased micron $SmCo_5$ powder combined with NMP binder in PVDF and dried on a copper foil. The only successful CV was collected from a slurry made with ball milled $SmCo_5$. This result is shown in Figure 4.8.

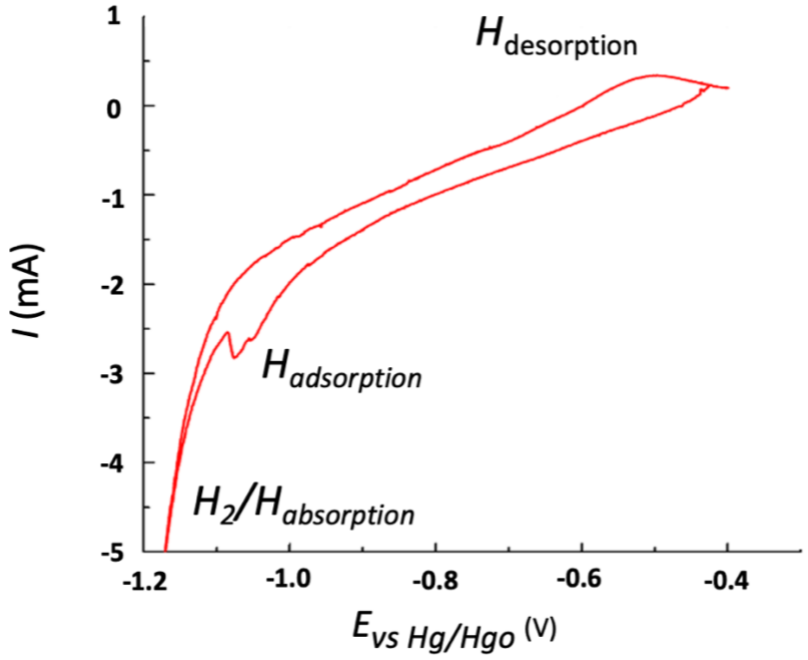

Figure 4.8. Cyclic Voltammogram of $SmCo_5$ electrode showing hydrogen adsorption, absorption, water splitting, and hydrogen desorption from an $SmCo_5$ electrode in 1 M KOH with a Pt wire counter electrode and Hg/Hgo reference.

This is a promising initial result, showing clear adsorption, absorption and desorption peaks. However, the peaks are underwhelming in comparison to the result of Ye et al., suggestion that only marginal hydrogenation was achieved. Furthermore, the overall current is much lower than expected, which is a clear sign that very little active material was accessible in this reaction.

The disappointing performance of even the best $SmCo_5$ electrode may be due to many factors. The first is that the consistency of the slurry was quite inhomogeneous due to the size of the particles and the magnetic attraction between them. This prevented an even mixing and spreading of the slurry, which may have caused a large portion of the active material to end up on the inside of binder-confined balls, thus greatly depleting the amount of material accessible to the electrolyte. Furthermore, while Ye et al. applied ~100 MPa to compress their particle slurry and fix it to their current collector, we did not apply any pressure when finishing our electrode.[5] This may have had

two deleterious effects. First, the separation of particles may have prevented hydrogen from moving into deeper layers of the slurry by failing to provide adequate transport channels. Second, without compression, the slurry was likely not making adequate contact with the current collector, .

The same procedure was repeated with Sm_2Co_{17} as the active material, but this time a solid ingot was used as the working electrode. The CV produced via this method is shown in Figure 4.9.

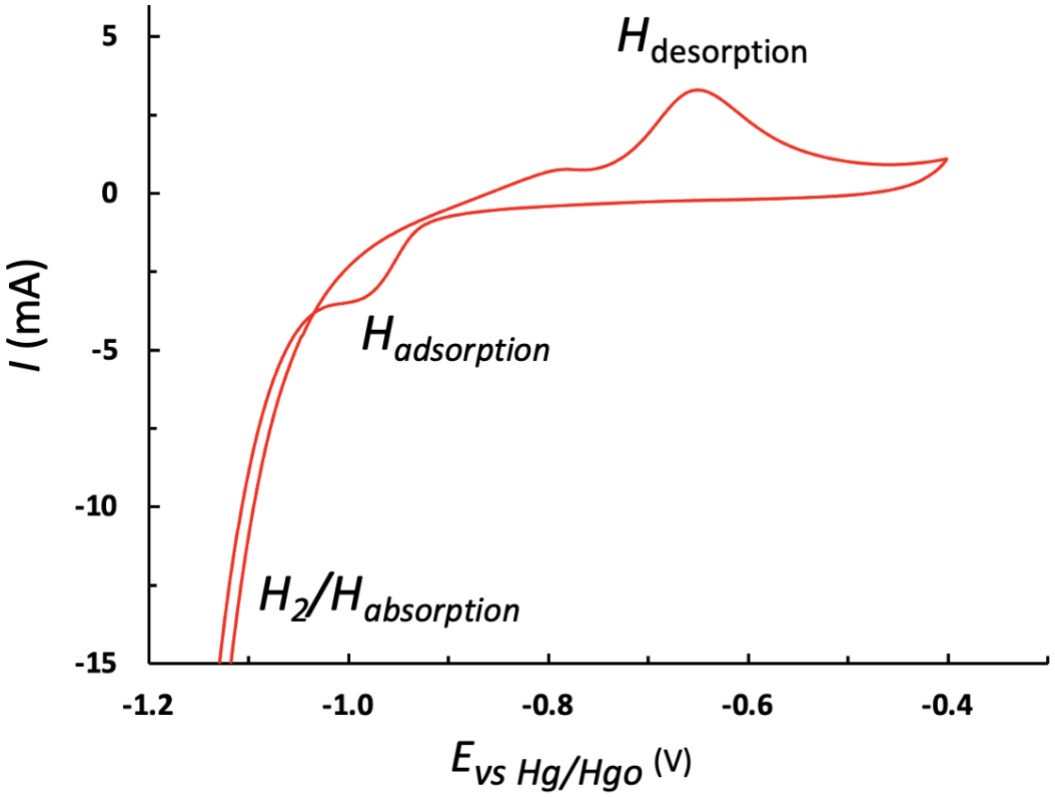

Figure 4.9. Cyclic Voltammogram showing hydrogen adsorption, absorption, water splitting, and hydrogen desorption from a Sm_2Co_{17} solid ingot electrode in 1 M KOH with a Pt wire counter electrode and Hg/Hgo reference.

This CV much more closely mimics that of $SmCo_5$ produced by Ye et al. Peaks coinciding with hydrogen adsorption, absorption, and desorption can be obviously distinguished. There is also

a slight oxidation peak around -0.8 V that is unaccounted for. This could indicate the presence of other redox-active species.

Much of the poor $SmCo_5$ performance may be due to poor slurry construction, but the superior electrochemical hydrogenation of Sm_2Co_{17} shown here is still very interesting considering the less favorable kinetics of Sm_2Co_{17} hydride formation. The remainder of this work explores this result.

4.5.2 Ex situ hydrogenation

Ex-situ gas-phase hydrogenation of both materials was attempted and monitored with PXRD to more precisely establish the hydriding thermodynamics and kinetics of our alloys. Due to limitations in laboratory capabilities, the initial hydrogenation experiments were restricted to hydrogen pressures of 1 atm or less. The remaining experimental parameters, such as temperature and reaction time, were set based on previous reports regarding optimal hydrogenation conditions for both materials. These are detailed in section 4.4.4.

Of the two, $SmCo_5$ has been much more intensely investigated for applications in hydrogen storage. Since it has an equilibrium hydrogen pressure at room temperature is 4 atm, the β-phase hydride will not grow under 1 atm at room temperature. Instead, the α-phase solid solution will form between hydrogen and the metal alloy.

Although the solid solution formation will not cause peak splitting and changes in a diffraction pattern as a phase transformation would, the metal lattice will likely expand in order to accommodate hydrogen in the α-phase. Such a transition should be observable by diffraction peak shifting. However, it is revealed in Figure 4.10, that no expansion occurred.

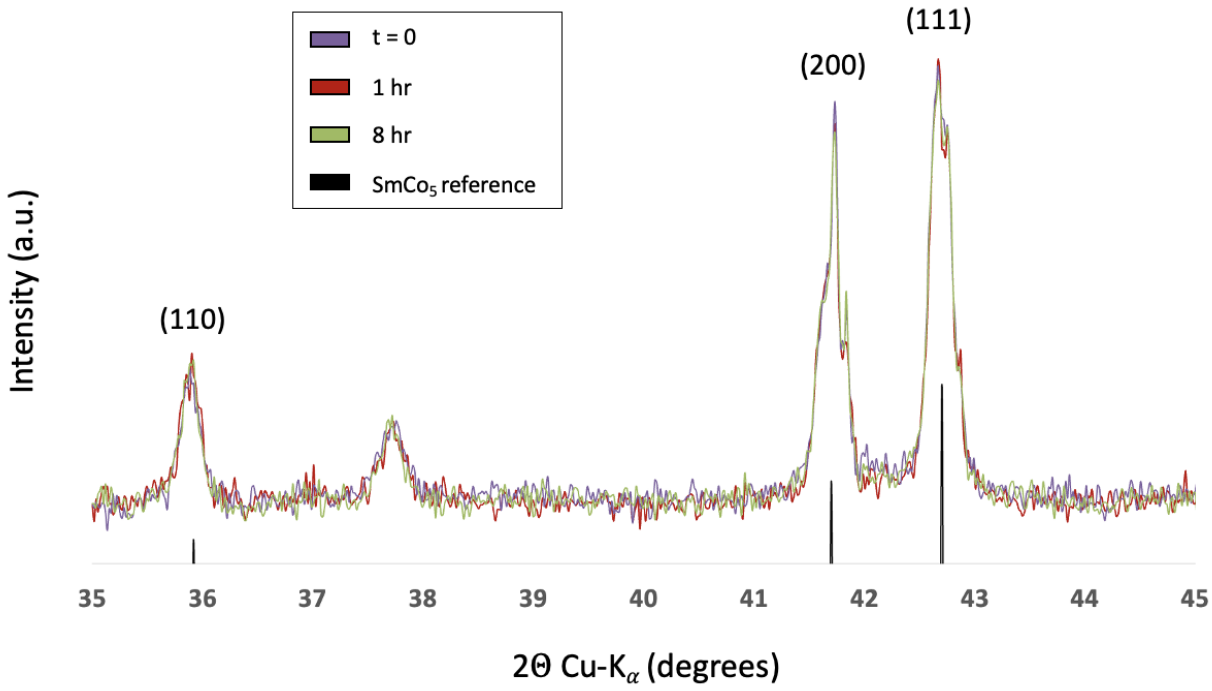

Figure 4.10. Powder X-ray diffraction patterns of $SmCo_5$ after 30 hours of hydrogenation under 1 atm at room temperature. No change in the crystal lattice was detected from immediately after hydrogenation (purple), one hour after (red), and 8 hours after (green).

The diffraction patterns collected following the attempted hydrogenation of $SmCo_5$ show no sign that any hydrogen was taken into the lattice. However, there may be several reasons that this observation was made that would not necessarily mean that hydrogenation to the α-phase was not accomplished during the exposure of $SmCo_5$ to hydrogen gas.

Although the dehydrogenation kinetics of the β-phase $SmCo_5$ hydride is notoriously slow, it may be much faster in the α-phase. Even if the α-phase hydride is retained for an appreciable time, because the lattice expansion in the α-phase is directly proportional to the amount of hydrogen per formula unit, it's possible that the expansion was not great enough to cause a diffraction peak shift noticeable beyond the noise.

Yet the more likely scenario is that the hydrogenation was not successful to any extent because the hydrogen pressure was simply insufficient to produce even a small amount of the α-phase. Although P-C-T curves suggest that 1 atm may be adequate for some small degree of hydrogenation, the materials used in these studies are always "activated" before the curve is collected.[23] In the activation process, the hydrogen storage material is subject to high hydrogen pressures, usually at elevated temperatures. This serves to prime the metal for hydrogenation in two ways. First, it ensures the destruction of any possible surface oxide layer so that the hydrogen gas applied in subsequent absorption-desorption cycles will be make direct contact with the metal. Second, the excessive hydrogen pressure creates cracks in the material and can even cause the metal to break down into smaller particles The result is faster kinetics due the increased surface area available for hydrogen absorption.[24]

Of the limited literature pertaining to the hydrogenation of Sm_2Co_{17}, none report an equilibrium hydrogen pressure because the existence of a β-phase Sm_2Co_{17} hydride has yet to be documented. This is likely a consequence of the extremely slow hydrogenation kinetics of Sm_2Co_{17} at lower temperatures necessitating thermodynamically unfavorable parameters.

The thermodynamics of hydride formation of both $SmCo_5$ and Sm_2Co_{17} favor lower temperatures due to the substantial negative entropy associated with the confinement of hydrogen gas within the metal lattice (as hydrogen atoms). Therefore, more favorable Gibbs free energies will result when temperature is low. This is why lower hydrogen pressures at low temperatures are required to achieve the same degree of hydrogenation as higher pressures at high temperatures. However, higher temperatures are favored kinetically, so a compromise must be reached.

Consider again the P-C-T curves of Sm_2Co_{17} and $SmCo_5$ (similar to $LaNi_5$, Figure 4.4) . It appears that the Sm_2Co_{17} P-C-T curve is only representative of the far-left portion of the $SmCo_5$ curves that correspond with the α-phase solid solution formation. The highest temperature isotherm

for the hydrogenation of $SmCo_5$ is taken at 80 °C, where the equilibrium hydrogen pressure is ~35 atm.[20] If the P-C-T curves of Sm_2Co_{17} follow a similar trend as those of $SmCo_5$, the equilibrium hydrogen pressure of Sm_2Co_{17} at 150 °C could exceed 200 atm.

Despite this, previous work demonstrated that the kinetics of Sm_2Co_{17} hydrogenation are entirely limiting below 150 °C, such that no hydrogen uptake occurs at all after 48 hours at 60 atm.[22] Therefore, the only worthwhile attempt at Sm_2Co_{17} hydrogenation under 1 atm hydrogen must be carried out at 150 °C for an extended period in hopes that some α-phase may be detected. According to the Sm_2Co_{17} P-C-T, this should result in an α-phase hydride with ~0.13 H/M. The resulting diffraction patterns are provided in Figure 4.11.

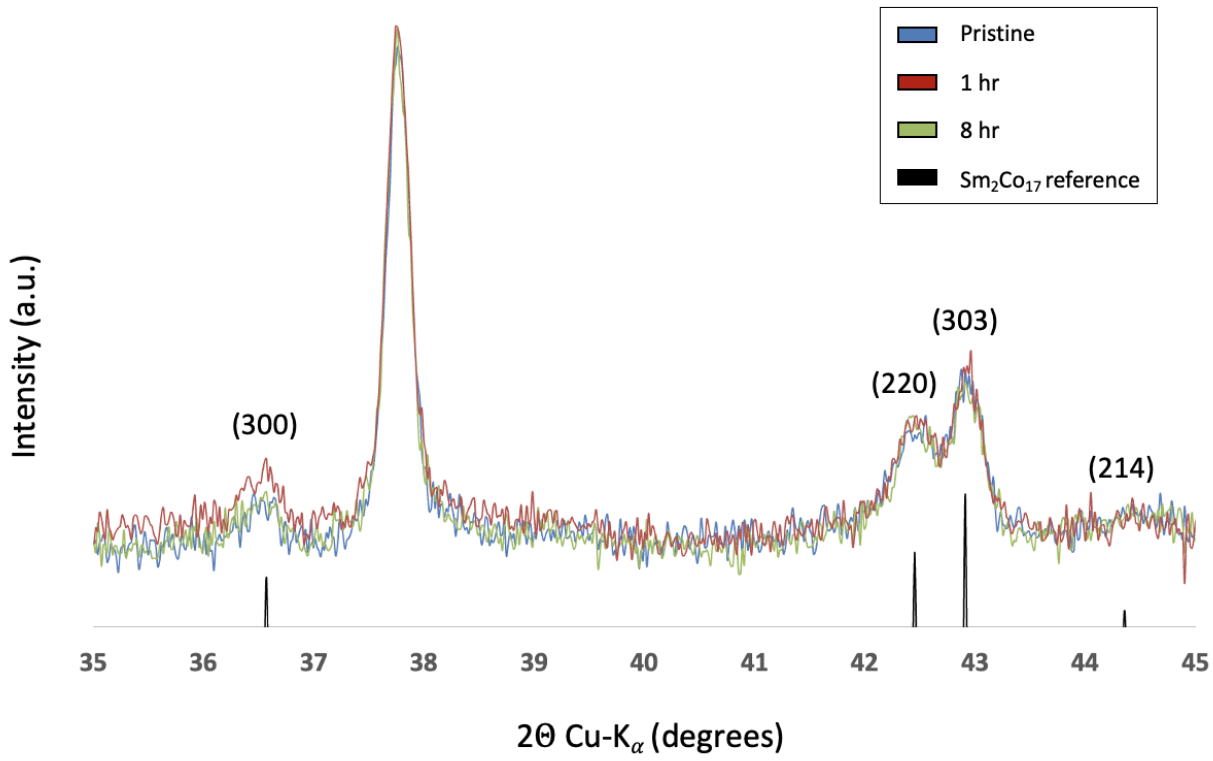

Figure 4.11. Powder X-ray diffraction patterns of Sm_2Co_{17} after 30 hours of hydrogenation under 1 atm at 150 °C. No change in the crystal lattice was detected from prior to hydrogenation (blue), one hour after (red), and 8 hours after (green).

Again, the diffraction patterns give no indication that Sm_2Co_{17} absorbed any hydrogen gas. Because the dehydrogenation of Sm_2Co_{17} is known to be slow despite only forming α-phase hydrides, this is likely due to the presence of an oxide layer barrier that is impenetrable to such low hydrogen pressures.

4.5.3 Addressing oxidation concerns with XPS

One major concern when working with the Sm-Co system is oxidation that may occur during exposure to air and/or the aqueous electrolyte. To explore the extent of this problem, the surface layers of air-exposed $SmCo_5$ and electrolyte-exposed Sm_2Co_{17} were characterized using X-ray photoelectron spectroscopy (XPS).

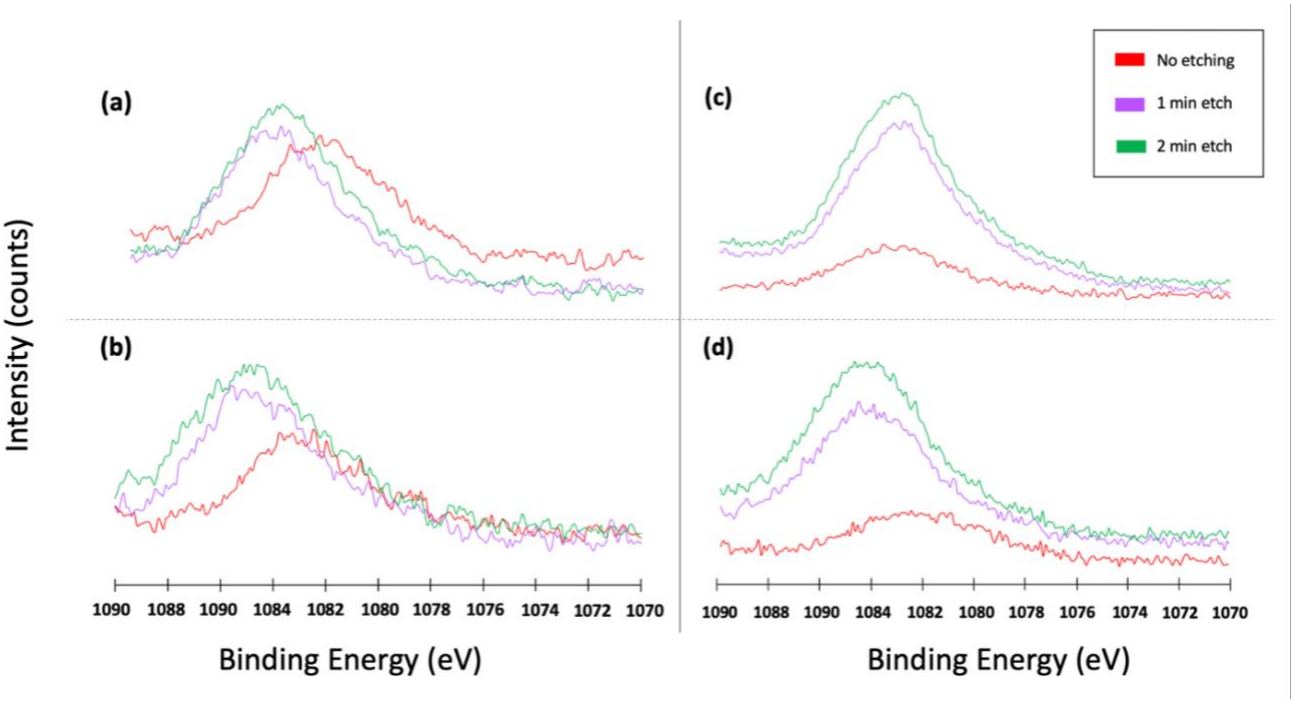

Figure 4.12 Normalized $3d_{5/2}$ photoelectron peaks corresponding to the Sm^{+3} state of (a) as-received $SmCo_5$ powder, (b) air-exposed $SmCo_5$ powder, (c) unused Sm_2Co_{17} ingot powder, and (d) used Sm_2Co_{17} ingot powder obtained immediately at the surface, after 1 minute of etching, and after 2 minutes of etching.

A clear shift in binding energy to higher values upon etching is observed in the as-received $SmCo_5$ powder (a), air-exposed $SmCo_5$ powder (b), and used Sm_2Co_{17} ingot powder (d). This shows

that there is a different electronic environment on the surface of these samples than there is in the bulk. The only sample that does not demonstrate this is the unused Sm_2Co_{17} ingot powder (d).

Other studies on the oxidation of Sm-Co magnets have reported a shift of the Sm^{+3} peak to lower binding energies upon oxidation.[26] The authors attribute this shift to an excess accumulation of Co on the outer surface changing the electronic environment of the Sm. According to this theory, Sm forms an internal oxide and is removed from the magnetic crystal lattice, freeing Co. This Co is then coaxed to the magnet's surface by a chemical potential gradient created by the oxygen chemisorbed there.

Relative to their more internal peaks, the air-exposed $SmCo_5$ surface peak (b, red) is shifted to lower binding energy to a greater extend than the as-received $SmCo_5$ (a). This is in accordance with the above theory since the air-exposed powder is presumably more oxidized than the as-received. However, the as-received surface peak is also shifted to a lower binding energy, suggesting that oxidation is a problem there as well. The same shift is seen in the used Sm_2Co_{17} spectrum, but not in the unused Sm_2Co_{17}, which indicates that there is very little or no oxide on the unused ingot.

It is also interesting to note the changes in peak height upon etching. In all the samples, the peaks become taller with longer etching. In other words, the sample surfaces produce less intense peaks for Sm^{+3} electrons. Because the peak height is proportional to the number of electrons detected at that binding energy, we can assume that the sample surface has less Sm^{+3} in comparison to the bulk. This trend in the $SmCo_5$ powders supports the idea that Sm forms internal oxides, resulting in a more Co-rich and Sm-poor surface because the presumably more oxidized 'air-exposed' powder has a significantly flatter unetched peak relative to its etched peaks. This height difference is not quite seen with the less oxidized 'as received' $SmCo_5$ powder.

Surprisingly, there is a massive height difference between the unetched and etched peaks of the unused Sm_2Co_{17} ingot powder. This lack of surface Sm^{+3} cannot be attributed to oxidation loss

because the surface peak doesn't display any shift to lower binding energies. Instead, this could be explained by the presence of a protective surface coating on the Sm_2Co_{17} ingot, which is commonly added in the manufacture of commercial rare earth magnets.

4.6 Conclusion

The Sm-Co system is highly promising for magnetic switching due to the massive magnetic changes possible by hydrogen charging. Although gas-phase hydrogenation is not pragmatic in electronic devices that this system is beneficial for, electrochemical hydrogenation can be accomplished with relatively low potentials.

Nanostructuring $SmCo_5$ and Sm_2Co_{17} can further improve upon unprecedented magnetic control demonstrated by Ye et al.[5,6] Toward this target, fundamental understandings of physical and magnetic structure, as well as the hydrogenation thermodynamics and kinetics of these Sm-Co alloys has been established.

The electrochemical hydrogen charging of a solid Sm_2Co_{17} ingot proved to work exceptionally well. However, charging of an $SmCo_5$ slurry electrode was poor, generating little current. This is likely in large part due to crude electrode assembly, with inhomogeneous slurry leaving much of the $SmCo_5$ inaccessible to the electrolyte. Future efforts should be made to improve slurry quality with smaller particles and to compress the dried electrode to ensure that the active material makes sufficient contact with itself and the current collector.

Attempts were made to hydrogenate powders under extremely mild conditions of 1 atm at room temperature and 150 °C for $SmCo_5$ and Sm_2Co_{17}, respectively. While these results were analyzed by ex-situ X-ray diffraction, which could have allowed the hydrogen to escape the structure prior to detection, the abundance of literature reporting slow dehydrogenation kinetics for these materials points to the hydrogenation being unsuccessful. This is presumably due to oxidation, a

problem that can be overcome by activating the materials under excess hydrogen pressures and elevated temperatures.

Oxidation of our samples was further explored with X-ray photoelectron spectroscopy. It was revealed that the pristine $SmCo_5$, air exposed $SmCo_5$, and used Sm_2Co_{17} ingot had undergone some oxidation. Although to a lesser extent, the oxidation of the pristine $SmCo_5$ indicates that better care must be taken toward air-free protocols. Meanwhile, the oxidation of the used Sm_2Co_{17} ingot may impede performance upon repeated cycling, presenting a future challenge in developing this technology.

4.7 References

(1) Bi, C.; Lui, Y.; Wang, W. G.; *et al. Phys. Rev. Lett.* **2014**, *113*, 267202.

(2) Bauer, U.; Yao, L.; Beach, G. S.; *et al. Nat. Mater.* **2015**,*14*, 174–181.

(3) Zhang, Q.; Luo, X.; Wu, H.; *et al. Nano Lett*. **2016**, *16*, 57.

(4) Tan, A. J.; Huang, M. Beach, G. S.; *et al. Nat. Mater.* **2019**, *18,* 35–41.

(5) Ye, X.; Singh, H.K.; Zhang, H. *et al. Nat. Commun.* **2020**, *11*, 4849

(6) Ye, X.; Yan, F.; Kruk, R.; *et al. Adv. Mater.* **2021**, *33*, 2006853.

(7) Zijlstra, H.; Westendorp, F. F. *Solid State Commun.* **1969**, *7*, 857–859.

(8) Sandrock, G. *J. Alloys Compd.* **1999**, *293*, 877-888

(9) Yan, A.; Bollero, A.; Gutfleisch O.; Müller, K.-H. *J. Appl. Phys.* **2002**, *91*, 2192-2196.

(10) Wallace, W. E. *U.S. Army Research.* **1980**, *ADA084943*

(11) Mosavati, N.; Young, K.-H.; Meng, T.; Ng, K. Y. S. *Batteries*, **2016**, *2*, 6.

(12) Jiang, X. Ph.D. Thesis, University of Nebraska-Lincoln, **2014**.

(13) Buschow, K. H.; van Diepen, A. M. *Solid State Commun.* **1974**, *15*, 903-906

(14) Kirchmayr, H. R.; Poldy, C. A. J. *Magn. Magn. Mater.* **1978**, *8*, 1-42.

(15) Coey, J. Magnetism and Magnetic Materials *Cambridge University Press*, **2009**

(16) Gutfleisch, O.; Müller, K.-H.; Khlopkov, K.; Wolf. M.; Yan, A.; Schäfer, R.; Gemming, T.; Schultz, L. *Acta Mater.* **2006**, *54*, 997-1008.

(17) Xiong, X. Y.; Ohkubo, T.; Koyama, T.; Ohashi, K.; Tawara, Y.; Hono, K. *Acta Mater*, **2004**, *52*, 737-748.

(18) Duerrschnabel, M.; Yi, M.; Uestuener, K.; Liesegang, M.; Katter, M.; Kleede, H.-J.; Xu, B.; Gutfleisch, O.; Molina-Luna, L. *Nat. Commun*. **2017**, *8*, 54.

(19) Schlapbach, L.; Züttel, A. *Nature*. **2001**, *414*, 353-358

(20) van Vucht, J. H.; Kuijpers, F. A.; Bruing, H. C. *Philips Res. Repts.* **1970**, *25*, 133-140.

(21) Eldosouky, A.; Škulj, I.; *J. Sustain. Metall.* **2018**, *4*, 516-527.

(22) Evans, J.; King, C. E.; Harris, I. R. *J. Mater. Sci.* **1985**, *20*, 817-820.

(23) Buschow, K. H. Handbook on the Physics and Chemistry of Rare Earths. *Eleveir,* **1984**, 6, 18-20.

(25) Dreistadt, D. M.; Le, T.-T.; Capurso, G. *et al. J. Alloys Compd.* **2022**, *919*, 165847.

(26) Mittireddi, R. T.; Sing, R. K.; Randa, E. *Corros. Sci.* **2021**, *190*, 109647